JOURNAL OF AIRCRAFT
Vol. 39, No. 5, September–October 2002

Free-Vortex Filament Methods for the Analysis of Helicopter Rotor Wakes

J. Gordon Leishman*
University of Maryland, College Park, Maryland 20742
Mahendra J. Bhagwat†
Advanced Rotorcraft Technology, Mountain View, California 94043
and
Ashish Bagai‡
Sikorsky Aircraft Corporation, Stratford, Connecticut 06615

The theoretical basis and the numerical implementation of free-vortex filament methods are reviewed for application to the prediction and analysis of helicopter rotor wakes. The governing equations for the problem are described, with a discussion of finite difference approximations to these equations and various numerical solution techniques. Both relaxation and time-marching wake solution techniques are reviewed. It is emphasized how the careful consideration of stability and convergence (grid-independent behavior) are important to ensure a physically correct wake solution. The implementation of viscous diffusion and filament straining effects are also discussed. The need for boundary condition corrections to compensate for the inevitable wake truncation are described. Algorithms to accelerate the wake solution using velocity field interpolation are shown to reduce computational costs without a loss of accuracy. Several challenging examples of the application of free-vortex filament methods to helicopter rotor problems are shown, including multirotor configurations, flight near the ground, maneuvering flight conditions, and descending flight through the vortex ring state.

Nomenclature

A	=	rotor disk area, πR^2, m^2
C_P	=	rotor power coefficient, $P/\rho A(\Omega R)^3$
C_{P_i}	=	induced power coefficient, $P_i/\rho A(\Omega R)^3$
C_{P_0}	=	profile power coefficient, $P_0/\rho A(\Omega R)^3$
C_T	=	rotor thrust coefficient, $T/\rho A(\Omega R)^2$
C_{T_h}	=	hovering rotor thrust coefficient, $T_h/\rho A(\Omega R)^2$
c	=	rotor blade chord, m
D	=	finite difference operator
h	=	perpendicular distance from vortex element to Lagrangian marker, m
N	=	number of helical vortex filaments
N_b	=	number of blades
n	=	time-integration index
P	=	rotor shaft power, W
P_h	=	ideal rotor-induced power in hover, $T^{3/2}/\sqrt{(2\rho A)}$, W
P_i	=	rotor-induced power, W
P_0	=	rotor profile power, W
p	=	rotor roll rate, rad · s^{-1}
q	=	rotor pitch rate, rad · s^{-1}
R	=	rotor radius, m
$\boldsymbol{r}$	=	position vector of a Lagrangian marker, m
r_c	=	core radius of vortex filament, m
T	=	rotor thrust, N
T_h	=	hovering rotor thrust, N
t	=	time, s
$\boldsymbol{V}$	=	velocity vector at a Lagrangian marker, ms^{-1}
V_c	=	axial (vertical) climb velocity, ms^{-1}
$\boldsymbol{V}_{\text{ex}}$	=	external velocity field, ms^{-1}
$\boldsymbol{V}_{\text{ind}}$	=	induced velocity, ms^{-1}
V_r, V_θ, V_z	=	radial, swirl, and axial velocities, respectively, ms^{-1}
$\boldsymbol{V}_\infty$	=	freestream velocity, ms^{-1}
v_i	=	average induced velocity, ms^{-1}
x, y, z	=	Cartesian coordinates, m
Γ	=	vortex filament circulation (strength), m^{2}s^{-1}
Γ_v	=	tip vortex circulation (strength), m^{2}s^{-1}
$\Delta\zeta$	=	vortex age discretization, rad
$\Delta\psi$	=	azimuthal discretization, rad
ζ	=	wake age, rad
κ_{ov}	=	induced power rotor overlap factor
λ_c	=	climb velocity ratio, $V_c/\Omega R$
λ_0	=	average inflow coefficient
μ	=	advance ratio, $V_\infty/\Omega R$
ν	=	kinematic viscosity of fluid, m^{2}s^{-1}
σ	=	eigenvalue of time-integration method, s^{-1}
ψ	=	azimuth angle, rad
ψ_b	=	blade azimuth, Ωt, rad
Ω	=	rotational velocity of rotor, rad · s^{-1}
ω	=	vorticity, m^{2}s^{-1}

Received 15 August 2001; revision received 3 May 2002; accepted for publication 14 May 2002.

*Professor, Department of Aerospace Engineering; leishman@eng.umd.edu. Senior Member AIAA.
†Aerospace Engineer; bhagwat@flightlab.com. Member AIAA.
‡Senior Aerodynamicist, Engineering Sciences; abagai@sikorsky.com. Senior Member AIAA.

Introduction

THE ability to define and predict accurately the aerodynamic environment at a helicopter rotor is essential for the design of better helicopters with improved aerodynamic performance, lower vibration levels, increased agility and maneuver capabilities, and less obtrusive rotor noise. The concentrated vortices that are trailed from the blade tips are the most dominant structures inside a helicopter rotor wake,[1] and it is the strengths, structure, and locations of these primary flow features that must be represented accurately by wake models. Whereas there are other significant vortical components comprising the rotor wake such as the inboard vortex sheet trailed from the blades, the tip vortices contribute the most to the local flow velocities and significantly impact the definition of the

aerodynamic environment at the blades. Because uncertainties in the prediction of rotor airloads propagate directly into design risk and aircraft development costs, great emphasis has been placed on improving the predictive capabilities of rotor wake and tip vortex models that are used in the design of advanced helicopters.

The use of modern, first-principles-based computational fluid dynamics (CFD) methods for the rotor wake has made some recent inroads toward a better definition of the detailed flow environment at the rotor blades, especially near the blade tip, where three-dimensional flow and compressibility effects dominate the problem.[2–4] Yet, the high computational costs and numerical limitations encountered with CFD methods in preserving concentrated vorticity (e.g., Ref. 5) have, so far, delayed the application of CFD to many practical problems that require an accurate treatment of the rotor wake. Another class of methods, called vortex methods, is an excellent alternative to CFD-based rotor wake methods. Although in the last 20 years or so, general vortex methods have become popular tools for the analysis of a wide range of aerodynamic problems,[6,7] as early as 1965 helicopter analysts recognized and explored the potential of vortex filament methods for the analyses of helicopter rotor wakes.[8]

In the application to helicopter rotor wakes, vortex filament methods have encompassed a variety of different approaches. These range from prescribed vortex techniques, where only the trailed vortices are specified a priori based on semi-empirical rules to more rigorous but computationally more demanding free-vortex or "free-wake" methods, where the vortical elements are allowed to follow force-free paths in accordance with the equations governing their convection. Although computationally efficient, prescribed vortex methods[9–11] are strictly limited in scope to hovering and level forward flight conditions that encompass the range of measured conditions for which they were originally formulated. Therefore, prescribed wake methods become much less useful as predictive tools under many flight conditions of practical interest, such as descending flight, flight near the ground, and for various types of maneuvers. Free-vortex methods, at least in principle, have fewer fundamental limitations and can be used to model more challenging flight conditions.

Free-vortex methods are based on a discrete representation of the rotor vorticity field and a Lagrangian representation of the governing equations for the wake elements and, when solved, determine the advancement of the elements through the flow. In essence, the wake elements are allowed to convect and deform under the action of the local velocity field to force-free locations. Such vortex methods have several advantages, including the inherent adaptivity of the computational elements to the vortical flow regions. Pioneering work in the application of free-vortex filament methods to rotor wake problems have been conducted by Crimi,[8] Clark and Leiper,[12] Scully,[13,14] and others,[15,16] and over the past three decades, several different numerical approaches to the free-wake problem have been developed. It is fair to say, however, that the predictive success of such methods has been considered somewhat mixed. This is, in part, because of various inherent numerical issues in solving the wake equations and also because a full assessment of their capabilities requires compatible levels of modeling fidelity for the blade motions and aeroelastic deformations (e.g., Ref. 17), as well as equivalent models for the nonlinear, unsteady airloads and initial wake rollup (tip vortex formation) formation behind the blades.[18–20]

The convection of the vortex elements through the rotor flowfield is the primary task handled by vortex methods, and a discussion of the numerical methods used to solve this transport problem is the main focus of the present paper. The methodology may also include some representation of viscous diffusion, vorticity intensification through the stretching of the vortex filaments, and possibly viscous dissipation. The representation of viscous effects in vortex wake methods is usually based on the use of semi-empirical rules (e.g., Ref. 21). However, the ability to integrate properly the convection of vorticity in a form consistent with viscous effects is an aspect of the problem that is critical for accurate predictions of the rotor wake geometry and its induced velocity field.[22] Although it will become clear from the examples shown that free-vortex filament models used for helicopter rotor wake analyses have now reached a good level of maturity and predictive capability, further improvements in numerical techniques and more thorough validation of the methods with experiments are still required.

Methodology

Governing Equations for the Rotor Vortex Wake

A description of the vorticity field in the rotor wake is governed by the three-dimensional, incompressible, Navier–Stokes equations, and can be represented in a velocity–vorticity ($\boldsymbol{V}, \boldsymbol{\omega}$) formulation[7] as

$$\frac{\partial \boldsymbol{\omega}}{\partial t} = -\underbrace{(\boldsymbol{V}\cdot\nabla)\boldsymbol{\omega}}_{\text{convection}} + \underbrace{(\boldsymbol{\omega}\cdot\nabla)\boldsymbol{V}}_{\text{strain}} + \underbrace{\nu\Delta\cdot\boldsymbol{\omega}}_{\text{diffusion}} \tag{1}$$

This equation defines the change of vorticity of a fluid element moving with the flow in terms of the instantaneous value of vorticity $\boldsymbol{\omega}$ and the local velocity field $\boldsymbol{V}$. The terms on the right-hand side (RHS) of Eq. (1) correspond to convection, strain, and diffusion of vorticity, respectively.

In many practical problems, it can be justified that viscous phenomena will be confined to much smaller length scales compared to potential flow phenomena. Therefore, vortex models use a Lagrangian description of the flow with discrete line vortices to represent concentrated lines of vorticity. This means that all of the vorticity is concentrated along the axis of each vortex filament, forming a vortex line singularity. Under incompressible, inviscid, irrotational conditions, vortex lines move as material lines, and their motion is described by the motion of Lagrangian fluid markers. The equations governing the behavior of these vortex filaments, therefore, reduce to a much simpler convection (advection) equation of the form

$$\frac{\mathrm{d}\boldsymbol{r}}{\mathrm{d}t} = \boldsymbol{V}, \qquad \boldsymbol{r}(t=0) = \boldsymbol{r}_0 \tag{2}$$

where $\mathbf{r}$ is the position vector of the point on the vortex filament, $\boldsymbol{r}_0$ is the initial position vector of the point, and $\boldsymbol{V}(\boldsymbol{r})$ is the local fluid velocity at the point $\boldsymbol{r}$. Although a simple equation, the significant complication in its solution is because of the highly nonlinear velocity field $\boldsymbol{V}$, which results from the self and mutually induced velocities of the entire vortex wake, as well as any external velocity field (both spatially and temporally).

In a typical (discretized) free-vortex filament scheme, Lagrangian markers are placed on contiguous vortex filaments trailing from the blades. Finding a solution for the motion of these markers, along with changes in the vorticity of the filaments, defines the problem. Any two successive markers on the vortex filaments must be linked together, for which the most natural and simplest is a piecewise linear reconstruction (Fig. 1).

Notice that, because of the helicoidal nature of a helicopter rotor wake, the filaments are relatively long and the number of markers per filament can be very large. This makes the tracking of the

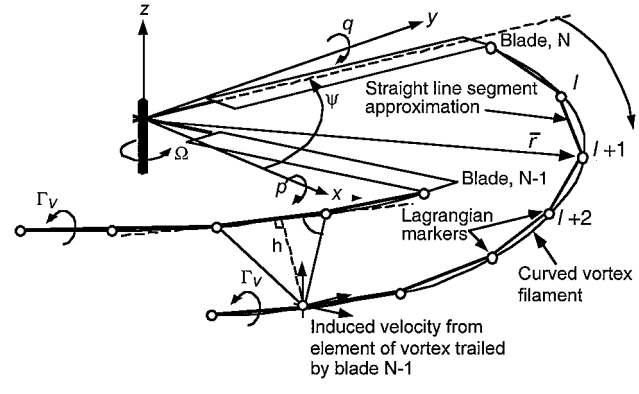

Fig. 1 Schematic of rotor coordinate system and the Lagrangian discretization of the vortex filaments that are trailed from the blade tips.

markers computationally demanding in most cases. Furthermore, numerous vortex filaments may be trailed along the blade span, with their initial strengths and locations being defined by a lifting-line or lifting-surface type of model. However, in the interests of retaining the practical levels of computational efficiency that are required for use in many applications, the vortex filament scheme is often implemented to represent only the behavior of the tip vortices. In this case, a viscous tip vortex rollup model may be implemented (discussed later).

For the rotor problem, the relationship in Eq. (2) can be formalized as

$$\frac{\mathrm{d}\boldsymbol{r}(\psi,\zeta)}{\mathrm{d}t} = \boldsymbol{V}[\boldsymbol{r}(\psi,\zeta)] \tag{3}$$

where $\boldsymbol{r}(\psi,\zeta)$ defines the position vector of a marker lying on a vortex filament that is trailed from a rotor blade located at an azimuth ψ at time t (Fig. 1). Let t_{ζ_0} be the time when the element was first formed and when the blade was located at $(\psi-\zeta)$. Because $\psi=\Omega t$ and $(\psi-\zeta)=\Omega t_{\zeta_0}$, then $\zeta=\Omega(t-t_{\zeta_0})$. The left-hand side (LHS) of Eq. (3) can be rewritten in terms of ψ, ζ, and Ω as

$$\frac{\mathrm{d}\boldsymbol{r}(\psi,\zeta)}{\mathrm{d}t} \equiv \frac{\partial \boldsymbol{r}(\psi,\zeta)}{\partial\psi}\frac{\mathrm{d}\psi}{\mathrm{d}t} + \frac{\partial \boldsymbol{r}(\psi,\zeta)}{\partial\zeta}\frac{\mathrm{d}\zeta}{\mathrm{d}t}$$

$$= \Omega\left[\frac{\partial \boldsymbol{r}(\psi,\zeta)}{\partial\psi} + \frac{\partial \boldsymbol{r}(\psi,\zeta)}{\partial\zeta}\right] \tag{4}$$

and so Eq. (3) reduces to a partial differential equation (PDE) of the form

$$\frac{\partial \boldsymbol{r}(\psi,\zeta)}{\partial\psi} + \frac{\partial \boldsymbol{r}(\psi,\zeta)}{\partial\zeta} = \frac{1}{\Omega}\boldsymbol{V}[\boldsymbol{r}(\psi,\zeta)] \tag{5}$$

Equation (5) defines the governing equation for the free-vortex problem applied to the rotor wake.

Notice that the LHS of Eq. (5) is a one-dimensional wave equation. The characteristic lines for the problem can be determined from the general solution of the linearized PDE in Eq. (5) by setting the RHS = const. These characteristic lines are oriented at an angle of 45 deg, requiring $\mathrm{d}\zeta/\mathrm{d}\psi=1$, that is, $\Delta\psi=\Delta\zeta$, and define directions of information propagation along which the finite difference equation becomes an ordinary differential equation (ODE).

The complexity in the solution to Eq. (5), however, arises from the velocity term on the RHS, which is a highly nonlinear function of the rotor wake geometry. The total induced velocity field at each Lagrangian marker is determined by the aggregate of the relative freestream velocity, the contributions induced by all of the other vortex filaments in the rotor wake, as well as the induced velocities produced by the blades, and any other sources of external velocities.

It will be appreciated that the rotor wake solution must also be coupled with the aerodynamic loading on the rotor blades, as well as accounting for rigid and elastic blade motions (blade dynamics) such as flapping and bending, lead/lag or in-plane motions, and cyclic pitch changes. In most cases, the rotor will need to be trimmed to a specific operating state, for example, rotor thrust and disk orientation, by the application of blade pitch inputs through pilot controls. This means that boundary conditions must be specified to ensure that the physics of the problem are correctly modeled. Specifically, all of the vortex filaments convected into the rotor wake must originate at the locations of the blade(s) with appropriate initial strengths, and this is often done with the use of lifting-line or lifting-surface models. In the case of a single rolled-up tip vortex from each blade, the viscous-dominated tip vortex rollup and the resulting initial values of the velocity field close to the vortex core are modeled semi-empirically. The prediction of tip vortex formation consistently with the blade airloads, especially with advanced tip shapes, is one of formidable complexity, and Rule and Bliss[20] give a good overview of the fundamentals.

Discretization of the Governing Equation

A numerical solution to the rotor wake problem dictates a discretization of both the LHS and the RHS of the governing equation, which must be performed in a manner that will ensure a consistent order of approximation between both sides. The discretization of the governing PDEs results in a set of finite difference equations (FDEs) that can be solved using numerical integration techniques (discussed later). The formulation of an integration methodology that is numerically robust (accurate, stable, versatile, and computationally efficient), however, is not an easy task.

LHS of the Governing Equation

The partial derivatives on the LHS of Eq. (5) must be discretized in the two domains, ψ and ζ. This is done by dividing the rotor azimuth domain into a finite number of angular step sizes of $\Delta\psi$ around the rotor azimuth. The wake vorticity is then segmented spatially along the vortex filament into curvilinear elements of equal angular increments of step $\Delta\zeta$ (Fig. 1). A discretized form of the LHS of Eq. (5) can be written in finite difference form as

$$D_\psi + D_\zeta \approx \frac{\partial \boldsymbol{r}}{\partial\psi} + \frac{\partial \boldsymbol{r}}{\partial\zeta} \tag{6}$$

where D is a finite difference operator. Ideally, Eq. (6) must be consistent with the PDE in that in the limiting case of zero discretization it approaches exactly the two derivatives being approximated.

One simple approach to finding an approximation to Eq. (6) would be to use a simple backward difference about point $\boldsymbol{r}(\psi,\zeta)$ such that

$$D_\psi = \frac{\boldsymbol{r}(\psi,\zeta)-\boldsymbol{r}(\psi-\Delta\psi,\zeta-\Delta\zeta)}{\Delta\psi} \tag{7}$$

with a similar equation for D_ζ. Although simple, this solution is only first-order accurate and would give unacceptably large errors in the wake solution. Despite this, this simple approach has seen some use in rotor wake analyses, with the numerical issues being suppressed by external damping or overrelaxation approaches.

The relaxation-based free-vortex wake analysis of Crouse and Leishman[23] and Bagai and Leishman[24] is based on finding both derivatives D_ψ and D_ζ in Eq. (6) at the midpoint of a grid cell using the values at surrounding grid points. Crouse and Leishman[23] use a three-point scheme, whereas Bagai and Leishman[24] use a five-point difference approximation, which helps enhance numerical stability. The stencil for the latter scheme is shown in Fig. 2a and results in

$$D_\psi \approx \left.\frac{\mathrm{d}\boldsymbol{r}}{\mathrm{d}\psi}\right|_{\psi+\Delta\psi/2,\zeta+\Delta\zeta/2} =$$

$$\frac{[\boldsymbol{r}(\psi+\Delta\psi,\zeta+\Delta\zeta)-\boldsymbol{r}(\psi,\zeta+\Delta\zeta)]+[(\boldsymbol{r}(\psi+\Delta\psi,\zeta)-\boldsymbol{r}(\psi,\zeta)]}{2\Delta\psi} \tag{8}$$

with an analogous approximation for the spatial derivative D_ζ.

To find the order of accuracy of this particular FDE, each term can be expanded as a Taylor series around the cell evaluation point at $\boldsymbol{r}(\psi+\Delta\psi/2,\zeta+\Delta\zeta/2)$ to give

$$D_\psi + D_\zeta = \frac{\partial \boldsymbol{r}}{\partial\psi} + \frac{\partial \boldsymbol{r}}{\partial\zeta} + \left(\frac{1}{24}\frac{\partial^3\boldsymbol{r}}{\partial\psi^3} + \frac{1}{8}\frac{\partial^3\boldsymbol{r}}{\partial\psi^2\partial\zeta}\right)\Delta\psi^2$$

$$+ \left(\frac{1}{24}\frac{\partial^3\boldsymbol{r}}{\partial\zeta^3} + \frac{1}{8}\frac{\partial^3\boldsymbol{r}}{\partial\psi\partial\zeta^2}\right)\Delta\zeta^2 + \cdots \tag{9}$$

It is apparent that the leading terms in the expansion of the difference approximations are of the order of $\mathcal{O}(\Delta\psi^2)$ and $\mathcal{O}(\Delta\zeta^2)$, so that this central difference approximation to the governing equation for the wake is second-order accurate in both ψ and ζ.

It is of further significance in this case to show that, for the homogeneous form of Eq. (5), the mixed derivatives in Eq. (9) can be written as $\partial^3\boldsymbol{r}/\partial\psi\partial\zeta^2 = -\partial^3\boldsymbol{r}/\partial\psi^3$, $\partial^3\boldsymbol{r}/\partial\psi^2\partial\zeta = \partial^3\boldsymbol{r}/\partial\psi^3$, and $\partial^3\boldsymbol{r}/\partial\zeta^3 = \partial^3\boldsymbol{r}/\partial\psi^3$, so that the discretization error in Eq. (9) can be written as

$$\epsilon = \left(\frac{\Delta\psi^2}{24}\frac{\partial^3 r}{\partial\psi^3} - \frac{\Delta\psi^2}{8}\frac{\partial^3 r}{\partial\psi^3} + \frac{\Delta\zeta^2}{8}\frac{\partial^3 r}{\partial\psi^3} - \frac{\Delta\zeta^2}{24}\frac{\partial^3 r}{\partial\psi^3}\right) + \cdots \tag{10}$$

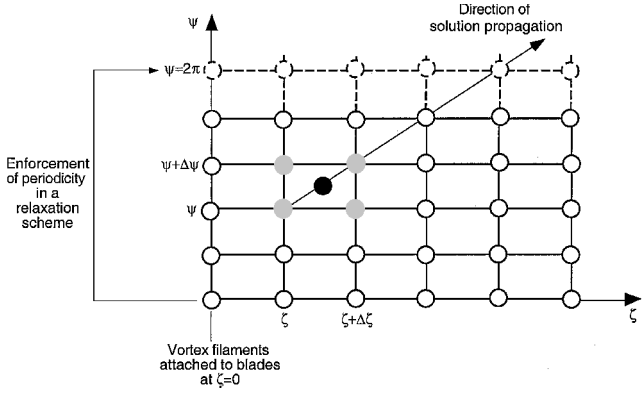

a) Five-point central difference stencil

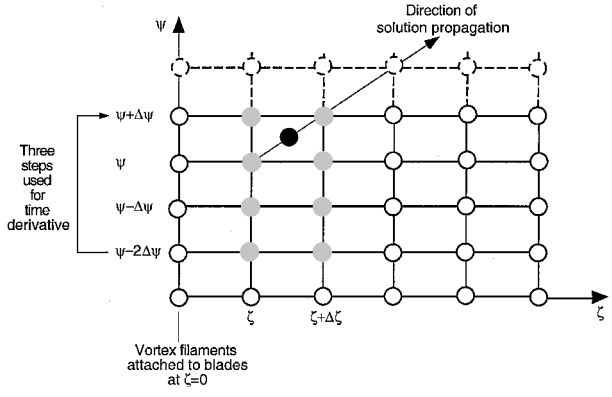

b) Backward difference stencil for time derivative

Fig. 2 Stencils for finite difference approximations to derivatives in governing equation for wake solution.

Because $\Delta\psi = \Delta\zeta$ in the physical problem, the finite difference scheme becomes exact because, as Eq. (10) shows, the truncation errors cancel.

The LHS of the discretized form of the governing equation in Eq. (6) can obviously be written in several other forms. In developing a time-accurate solution to the rotor wake problem, Bhagwat and Leishman[25] have used information at three previous time steps to approximate the D_ψ time derivative. In this case, the finite difference approximation [the predictor–corrector with second-order backward difference (PC2B) scheme] is

$$D_\psi \approx \frac{\partial \boldsymbol{r}(\psi + \Delta\psi/2, \zeta)}{\partial \psi}$$

$$= \frac{3\boldsymbol{r}(\psi + \Delta\psi, \zeta) - \boldsymbol{r}(\psi, \zeta) - 3\boldsymbol{r}(\psi - \Delta\psi, \zeta) + \boldsymbol{r}(\psi - 2\Delta\psi, \zeta)}{4\Delta\psi} \tag{11}$$

for which the stencil is shown in Fig. 2b. For this backward difference approximation, using a Taylor-series analysis about the evaluation point at $\boldsymbol{r}(\psi + \Delta\psi/2, \zeta)$ gives

$$D_\psi = \frac{\partial \boldsymbol{r}}{\partial \psi} - \left(\frac{5}{24}\frac{\partial^3 \boldsymbol{r}}{\partial \psi^3}\right)\Delta\psi^2 + \left(\frac{1}{4}\frac{\partial^4 \boldsymbol{r}}{\partial \psi^4}\right)\Delta\psi^3 + \cdots \tag{12}$$

Therefore, this approximation is second-order accurate in time at the evaluation point.

When this approximation for D_ψ is used along with the five-point central difference approximation for the spatial derivative D_ζ as earlier, the LHS of the governing equation can be written as

$$D_\psi + D_\zeta = \frac{\partial \boldsymbol{r}}{\partial \psi} + \frac{\partial \boldsymbol{r}}{\partial \zeta} + \left(-\frac{5}{24}\frac{\partial^3 \boldsymbol{r}}{\partial \psi^3} + \frac{1}{8}\frac{\partial^3 \boldsymbol{r}}{\partial \psi^2 \partial \zeta}\right)\Delta\psi^2$$

$$+ \left(\frac{1}{8}\frac{\partial^3 \boldsymbol{r}}{\partial \psi \partial \zeta^2} + \frac{1}{24}\frac{\partial^3 \boldsymbol{r}}{\partial \zeta^3}\right)\Delta\zeta^2 + \frac{1}{4}\frac{\partial^4 \boldsymbol{r}}{\partial \psi^4}\Delta\psi^3 + \cdots \tag{13}$$

where all of the derivatives are evaluated at the midpoint of the grid cell. The leading error terms in Eq. (13) are second-order in $\Delta\psi$ and $\Delta\zeta$, confirming the second-order accuracy for this scheme.

RHS of the Governing Equation

The contributing elements to the RHS of the governing equation in Eq. (5) need careful delineation and can be written as

$$\boldsymbol{V} = \boldsymbol{V}_\infty + \boldsymbol{V}_{\text{ind}} + \boldsymbol{V}_{\text{ex}} \tag{14}$$

The freestream velocity components $\boldsymbol{V}_\infty$ relative to the rotor generally constitute a simple velocity vector. The term $\boldsymbol{V}_{\text{ex}}$ can be considered as a general external velocity term, representing a variety of contributions including maneuver effects (discussed later).

The induced velocity term $\boldsymbol{V}_{\text{ind}}$ is the most complicated (and numerically expensive to evaluate) element of $\boldsymbol{V}$, comprising the self- and mutual-induced velocities from all of the vortical filaments in the rotor wake. The induced velocity at any point must be determined by integrating along the length of each curvilinear filament, and because the resulting integral cannot be evaluated exactly, it must be approximated by numerical summation with discrete vortex elements or segments. Several possible discretization schemes have been used for rotor wake analyses, including the use of vortex blobs,[26] vortex particles,[27] straight-line segmentation,[24,25,28,29] and curved vortex elements.[30] Another method, also using curved elements, which is called the constant vorticity contour approach,[31,32] is a alternative method worthy of note.

Straight-line segmentation of the vortex filaments is by far the most common form of discretization because the induced contribution of each vortex segment can be evaluated exactly from the well-known Biot–Savart law. The velocity induced at a point located at position $\boldsymbol{r}$ relative to a vortex element $\mathrm{d}\boldsymbol{l}$ is determined using

$$\boldsymbol{V}_{\text{ind}} = \frac{\Gamma}{4\pi}\left[\frac{h^2}{\left(r_c^{2n} + h^{2n}\right)^{1/n}}\right]\int \frac{\mathrm{d}\boldsymbol{l} \times \boldsymbol{r}}{|\boldsymbol{r}|^3} = \frac{\Gamma}{4\pi}K\int \frac{\mathrm{d}\boldsymbol{l} \times \boldsymbol{r}}{|\boldsymbol{r}|^3} \tag{15}$$

where h is the perpendicular distance of the evaluation point from the influencing vortex element (Fig. 1), r_c is defined as the core radius (discussed later), and Γ is the circulation strength of that vortex element. The factor K desingularizes the equation as $r \to 0$. The integer n in the K term in Eq. (15) defines the form of the velocity profile, which for rolled-up tip vortices may be defined based on empirical evidence.[21] [Note that if $n \to \infty$, the Rankine vortex profile is obtained. If $n = 1$, the Scully model[14] or Kaufmann model[33] is obtained, and if $n = 2$, then an algebraic approximation to the Lamb–Oseen vortex model (see Ref. 34) is obtained.]

The induced velocity from any segment can be written as $\boldsymbol{V}_{\text{ind}}(\psi_k, \zeta_l; \zeta_i)$, which represents the velocity at the Lagrangian marker at $\boldsymbol{r}(\psi_k, \zeta_l)$ induced by the ith straight-line vortex segment extending from $\boldsymbol{r}(\psi_k, \zeta_{i-1})$ to $\boldsymbol{r}(\psi_k, \zeta_i)$. Therefore, the net induced velocity at point $\boldsymbol{r}(\psi_k, \zeta_l)$ can be expressed as a sum over all vortex elements over all vortex filaments by using the summation equation

$$\boldsymbol{V}[\boldsymbol{r}(\psi_k, \zeta_l)]|_{\text{discrete}} = \sum_{n=1}^{N_b}\sum_{i=1}^{N_\zeta} \boldsymbol{V}_{\text{ind}}\left[\psi_k + (n-1)\frac{2\pi}{N_b}, \zeta_l; \zeta_i\right] \tag{16}$$

This type of summation by straight-line segmentation of the vortex filaments is analogous to trapezoidal quadrature, which can be shown to be second-order accurate for problems involving curved or circular elements.[29]

However, caution should always be employed with numerical integration schemes involving the Biot–Savart law. It was shown in Ref. 25 that for rotor wake problems the discretized evaluation of the induced velocity field usually also results in the inclusion of higher-order antidissipative terms into the solution. Such negative dissipation is nonphysical, and unless controlled by some positive numerical dissipation in the numerical solution to the LHS of the governing equation, these inherent antidissipative effects can result in unbounded, nonphysical growth of numerical disturbances.

Integration Schemes

It is important to develop numerically efficient methodologies with acceptably low computational overheads so that the wake models can be used in a variety of practical rotor applications. Whereas several integration techniques are possible, the choice of numerical scheme is usually a compromise between numerical accuracy, stability, and computational efficiency.

The discretization of the governing PDE for the rotor wake results in a governing equation that can be written in the representative form

$$\frac{\mathrm{d}r}{\mathrm{d}t} = Dr + V(r,t) \tag{17}$$

where D is the spatial discretization. One such equation applies to every Lagrangian marker in the rotor wake, effectively resulting in a system of simultaneous ODEs. In an Euler explicit integration scheme, a new solution for the wake is obtained by extrapolating from the previous step by means of a single, backward difference step, that is,

$$r_{n+1} = r_n + [Dr_n + V(r_n)]\Delta t \tag{18}$$

Although this scheme has seen some use in helicopter rotor wake applications, the scheme is only first-order accurate and results in the rapid accumulation of discretization errors. Therefore, this method becomes unstable, even with the addition of artificial numerical damping. An implicit difference scheme to solve the same equation involves current step information as

$$r_{n+1} = r_n + [Dr_{n+1} + V(r_{n+1})]\Delta t \tag{19}$$

In this case, information at the $(n+1)$th step has not yet been determined. Therefore, V must first be linearized using a Taylor expansion, resulting in what would be called a semi-implicit scheme. This approach was used in the free-vortex wake scheme developed by Miller and Bliss.[35] Although numerical errors are reduced with this technique, it becomes computationally very expensive in application because it requires the solution of a large set of simultaneous linear equations at each step.

A technique to improve the accuracy and stability of explicit schemes may be made by using predictor–corrector (PC) schemes, a point recognized by Crouse and Leishman,[23] without the need for artificial numerical damping. The predictor step is used mainly to obtain an intermediate solution at the new time step to enable the induced velocity calculations to proceed. However, a disadvantage of PC schemes is that they require two velocity field calculations per time step. In the PC approach, the corrected solution at the current nth step is obtained by averaging the induced velocity from the previous $(n-1)$th step with the predicted induced velocities from the current nth predictor step at the current step.

Predictor:

$$\tilde{r}_{n+1} = r_n + [Dr_n + V(r_n)]\Delta t \tag{20}$$

Corrector:

$$r_{n+1} = r_n + [D\tilde{r}_{n+1} + V(\tilde{r}_{n+1})]\Delta t \tag{21}$$

The enhanced stability and increased convergence rates of PC schemes generally outweigh the additional computational expense of performing two induced velocity calculations per step.

Another improvement to the PC scheme for the free-vortex problem was introduced in Refs. 24 and 36, resulting in what is known as a pseudoimplicit PC (PIPC) scheme, where the predictor is

$$\tilde{r}_{n+1} = r_n + [D\tilde{r}_{n+1} + V(r_n)]\Delta t \tag{22}$$

and the corrector is

$$r_{n+1} = r_n + \left\{Dr_{n+1} + \tfrac{1}{2}[V(\tilde{r}_{n+1}) + V(r_n)]\right\}\Delta t \tag{23}$$

It will be apparent that the explicit predictor step has been modified into a pseudoimplicit equation because the velocity field is calculated explicitly from the previous time step, yet the position vectors at the current (predictor) time step, $\tilde{r}_{n+1}$, also appear on the RHS. The predictor equation, therefore, is no longer fully explicit.[24,36] The corrector step incorporates an averaging scheme whereby an average of the velocity field from the previous time step and the predicted value are used to update the corrected position vectors. This helps to further improve the stability characteristics of the scheme and to enhance convergence. Once again, the position vectors at the current time step also appear on the RHS, as well as making the corrector step a pseudoimplicit equation.

Note that the velocity terms on the RHS of Eqs. (22) and (23) are still treated explicitly in that the final values for the induced velocities are computed using an average of those at the previous step and the predicted values from the current iteration. The position vectors $\tilde{\boldsymbol{r}}_{n+1}$ are predicted values returned by the explicit predictor step. The "pseudoimplicitness" of the PIPC results in a scheme in which information is propagated very rapidly through the computational domain.

Methods of Implementation

Two main classes of free-vortex wake solution methodologies for solving the governing equations have been developed, namely, iterative (or relaxation) methods and time-marching methods. Time-marching free-vortex methods potentially offer the best level of approximation to the rotor wake problem and with the fewest restrictions in application. However, these methods have proven susceptible to types of instabilities resulting from the initiation of numerical microstructures (Ref. 37), thereby reducing the confidence that a physically realistic solution has been obtained. Properly distinguishing between the known physical instabilities of rotor wakes[38] and those that are numerical in origin has proven to be a major hindrance in the development of reliable and robust time-accurate free-vortex wake models for helicopter rotor applications.[25]

Relaxation methods that explicitly enforce periodicity of the evolving wake are applicable only to steady-state problems, but are usually (but not always) found to be free of the numerical problems that are often associated with time-marching solutions. Such relaxation methods include influence-coefficient-based methods,[28,39] and semi-implicit[40] or pseudoimplicit methods.[24,36,41]

Relaxation Approach

Relaxation methods assume that the wake structure is globally periodic at the rotational frequency of the rotor. This assumption is imposed on the wake geometry by mapping the temporal coordinate ψ to a spatial coordinate with a periodic boundary condition. The governing equation for the wake in Eq. (5) is then modified to include a pseudotime term, that is,

$$\frac{\partial \boldsymbol{r}}{\partial \tilde{t}} + \frac{\partial \boldsymbol{r}}{\partial \psi} + \frac{\partial \boldsymbol{r}}{\partial \zeta} = \boldsymbol{V}(\boldsymbol{r}) \tag{24}$$

Equation (24) is solved in the pseudotime domain $\tilde{t}$ until a steady state is reached. Some form of classical numerical relaxation is used in the pseudotime integration. Note that the intermediate iterations, or pseudotime steps, do not have any physical significance. However, when the solution has converged and so does not change with $\tilde{t}$, the $\tilde{t}$ derivative in Eq. (24) vanishes, and the original governing equation (5) is recovered, albeit with periodicity in ψ.

In the implementation of the relaxation approach, the blade azimuth location ψ is frozen in time, and the positions of each Lagrangian marker on the vortex filaments are successively updated. The initial or starting induced velocity field is usually calculated based on a rigid or otherwise prescribed initial wake geometry, that is, $\boldsymbol{r}_0$ is defined a priori based on either the assumption of a rigid, undistorted wake, a semi-empirical approximation,[11,42] or some other previous solution. The position vector updates proceed using an integration scheme applied along the vortex filament length for each blade azimuth location.

The concept is shown in Fig. 2a, which shows the propagation of information in the computational domain. Note that each vortex filament is attached to its respective blade/near wake at its point of origin, which defines the boundary condition in the ζ direction,

and periodicity is assumed in the ψ direction. Further details of implementing boundary conditions are given in Refs. 24 and 36.

Like any relaxation scheme, it is necessary to impose a mathematical convergence criterion for this type of wake solution. Usually this is done based on a measure of the L_2 or L_∞ norm of the change in the wake geometry between successive iterations. Convergence is reached after the norm of the current iteration with respect to the first iteration drops below a certain prescribed threshold. The change in the norm must fall below this value to ensure that the wake structure has properly converged and the wake geometry exhibits no appreciable change between successive wake iterations, that is, a periodic solution has been reached. Relaxation methods for the rotor wake usually show rapid monotonic convergence characteristics under most flight conditions and so are generally computationally efficient.

Time-Marching Approach

There are many applications in helicopter aerodynamics for which relaxation methods are unsuitable because the physics of the rotor wake cannot be assumed globally periodic. Such unsteady environments include rotor wake/airframe interaction problems, operations near the ground, transient maneuvering flight conditions, autorotational flight, or when operating in descending flight through the vortex-ring state. In a time-marching algorithm, the time evolution of the position vectors of each wake Lagrangian marker can be expressed by

$$\frac{\mathrm{d}\boldsymbol{r}(\psi,\zeta)}{\mathrm{d}\psi} = D_\zeta + \boldsymbol{V}[\boldsymbol{r}(\psi,\zeta)]|_{\text{discrete}} = F[\boldsymbol{r}(\psi),\psi] \tag{25}$$

As already shown, a second-order, five-point central difference approximation can be used to find the spatial derivative ζ, and the RHS of Eq. (25) can be represented discretely as $F[\boldsymbol{r}(\psi),\psi]$. Time-marching algorithms can also take advantage of the numerical improvements produced by a PC sequence. Although any initial wake geometry can be specified from which to march the solution, the initial or starting induced velocity field is usually a relaxation solution. This helps minimize the transients (and numerical costs) associated with the initial condition that would otherwise be introduced into the time-marching solution

The stability of the time-integration algorithm is particularly important to ensure proper wake convergence. An issue in the solution of Eq. (25) is in the treatment of the time derivative ψ. As shown in Ref. 25, a linearized stability analysis can be used to understand the basic stability characteristics. To do this, a representative equation may be considered

$$\frac{\mathrm{d}r}{\mathrm{d}t} = \lambda r + a e^{\mu t} \tag{26}$$

where λ, μ, and a are constants. The exact solution to Eq. (26) is given by

$$r(t) = r(0)e^{\lambda t} + a[(e^{\mu t} - e^{\lambda t})/(\mu - \lambda)] \tag{27}$$

The solution is assumed to have the form $r^{n+1} = \sigma r^n$, and the solution for σ gives the eigenvalues of the time-marching algorithm. The linear stability criterion requires that the amplification factor for each time-step, that is, $|\sigma|$, must be less than or equal to unity, that is, $|\sigma(\lambda = i\omega\Delta t)| \le 1$, where Δt is the step size. This implies that the eigenvalues for $\lambda = i\omega\Delta t$ must always lie within the unit circle in the complex σ-plane.

The earlier described PC2B time-marching algorithm applied to the representative equation in Eq. (26) gives for the predictor

$$\tilde{r}_{n+1} = r_n + \tfrac{1}{2}\lambda\Delta t(\tilde{r}_{n+1} + r_n) + \tfrac{1}{2}a\Delta t e^{\mu n\Delta t} \tag{28}$$

and for the corrector,

$$3r_{n+1} = r_n + 3r_{n-1} - r_{n-2} + 2\lambda\Delta t(r_{n+1} + r_n) + 2a\Delta t\{\exp(\mu n\Delta t) + \exp[\mu(\widetilde{n+1})\Delta t]\} \tag{29}$$

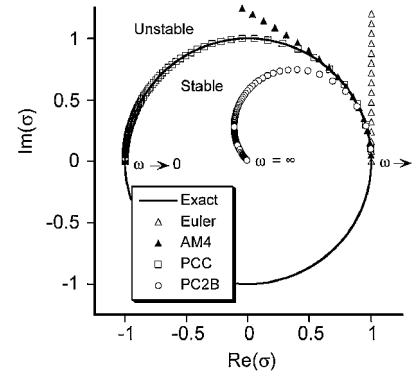

Fig. 3 Principal eigenvalues for four time-marching wake algorithms.

The eigenvalues are given by the solutions to the characteristic equation $(3 - 2\lambda\Delta t)\sigma^3 - (1 + 2\lambda\Delta t)\sigma^2 - 3\sigma + 1 = 0$. Because the time integration involves three time steps, at least in this case, there are three eigenvalues. The principal eigenvalue σ_1 is the most important for the accuracy of the solution, which is given by

$$\sigma_1 = 1 + \lambda\Delta t + \tfrac{1}{2}\lambda^2\Delta t^2 + \tfrac{1}{2}\lambda^3\Delta t^3 + \tfrac{1}{8}\lambda^4\Delta t^4 + \tfrac{1}{8}\lambda^5\Delta t^5 + \cdots \tag{30}$$

The first three terms in Eq. (30) indicate that the solution is second-order accurate in time.

The principal eigenvalue for the PC2B algorithm is shown in Fig. 3 as a function of discretization, along with the eigenvalues for three other representative time-marching algorithms. The forward Euler algorithm is a one-step explicit method and is given here as a reference because it has historically been used in several implementations of free-vortex wake schemes. The Adams–Moulton fourth-order (AM4) algorithm, which has been suggested by Jain and Conlisk,[43] is a good reference because like the preceding scheme it is also a two-step PC method. The PC with central difference (PCC) algorithm is another central-differencing scheme.[25] The results in Fig. 3 show that the explicit Euler method is inherently unstable for all levels of discretization because the eigenvalue always lies outside the unit circle. The AM4 algorithm is formally fourth-order accurate, with the eigenvalue closely following the unit circle for small values of $\omega\Delta t$, but it, too, is unstable, albeit only for larger values of $\omega\Delta t$. The PCC algorithm is always neutrally stable with no damping. Finally, the PC2B algorithm is shown to be stable for all values of discretization and with slightly positive damping.

As already mentioned, the equations governing the wake are highly nonlinear and, therefore, the foregoing linear stability analysis may only be considered indicative of the stability of the numerical algorithm. To better understand the stability of the nonlinear equations, modified equations corresponding to these algorithms can be examined. For example, a Taylor-series expansion shows that the PC2B algorithm is a second-order accurate approximation to the original governing equations, that is,

$$\frac{\partial \boldsymbol{r}}{\partial \psi} + \frac{\partial \boldsymbol{r}}{\partial \zeta} = \frac{\boldsymbol{V}(\boldsymbol{r})}{\Omega} + \mathcal{O}(\Delta\zeta^2) \tag{31}$$

Including more terms in the Taylor-series expansion of the discrete finite difference equations gives the so-called modified equations. For example, including up to fourth-order terms gives

$$\frac{\partial \boldsymbol{r}}{\partial \psi} + \frac{\partial \boldsymbol{r}}{\partial \zeta} = \frac{\boldsymbol{V}(\boldsymbol{r})}{\Omega} + \Delta\zeta^2[\text{dispersive terms}] + \Delta\zeta^3\,[\text{dissipative terms}] + \mathcal{O}(\Delta\zeta^4) \tag{32}$$

The finite difference equation is, therefore, a fourth-order accurate approximation to the modified equation. The numerical solution is also a fourth-order accurate approximation to the solution of the modified equation, while being only a second-order approximation to the solution of the original governing equation in Eq. (5). Therefore, the modified equations can be used to determine the stability of the numerical solution.

It was shown in Ref. 25 that the discretized evaluation of the induced velocities from the rotor wake usually results in the addition of higher-order antidissipative terms. Note that antidissipation is nonphysical and results in unbounded exponential growth of any numerical disturbances, that is, the modified equation itself is unstable. Therefore, numerical solutions obtained using the Euler explicit or AM4 algorithms, which do not provide any positive dissipation, also exhibit nonphysical instabilities. The PC2B algorithm is one class of algorithms that introduces additional dissipative terms into the modified equations. This effectively cancels the antidissipative terms, thereby making the equations stable.

Viscous Effects

In general, viscous phenomena are usually confined to much smaller length scales compared to potential flow phenomena. However, the epicycloidal structure of a helicopter wake geometry implies that the detailed viscous structure of concentrated vortices and vortex sheets can be important even at large length scales, for example, of the order of the rotor radius. In helicopter rotor flows, the preponderance of interactions between blades and wake vortex filaments means that the modeling of viscous effects and the velocity field near the filament core must go beyond ad hoc "cutoffs" or other approaches designed simply to desingularize numerically the Biot–Savart law. Typically, the viscous structure and associated diffusion of the vortical filaments is incorporated using semi-empirical models.[1] These models may be applied to individual vortex filaments (such as the vortex sheet) through the factor K in Eq. (15) or to the completely rolled-up tip vortex [which would use $\Gamma = \Gamma_v$ in Eq. (15)], and it should be recognized that different visocus models may be applied in each case.

Simple Lamb-like exponential or algebraic models for the rolled-up tip vortex are popular choices for K because these are computationally efficient and are known from correlation studies with experimental measurements to give good approximations to the structure of a concentrated tip vortex. A commonly used model for K is the algebraic model suggested by Kaufmann[33] and later by Scully.[14] This model represents the velocity distribution near the vortex core, but measurements suggest that it may underpredict the peak swirl velocity.[44,45] A general family of algebraic velocity models for K was proposed by Vatistas et al.,[46] for which certain models show good comparisons with the observed swirl velocities measured in rotor tip vortices.[21,24,47,48]

The viscous growth of the core of the vortex filaments with time t can be approximated by the Lamb–Oseen result that $r_c(t) = \sqrt{(4\alpha\nu t)}$, where $\alpha = 1.25643$. The tangential velocity for the Lamb–Oseen model as a function of distance r from the vortex axis can be written as

$$V_\theta(\bar{r}) = (\Gamma_v/2\pi r_c)\left[\left(1 - e^{-\alpha\bar{r}^2}\right)\Big/\bar{r}\right] \tag{33}$$

Squire[49] suggested an effective origin offset to give a finite vortex core at the origin of the tip vortex, a condition necessary in practice to avoid infinitely large velocities at $t = 0$. With the use of Squire's approach, the growth in the viscous core radius of a blade tip vortex relative to the blade at which it originated can be modeled by

$$r_c(\zeta) = \sqrt{4\alpha\delta\nu[(\zeta - \zeta_0)/\Omega]} \equiv \sqrt{r^2_{\text{initial}} + 4\alpha\delta\nu\zeta/\Omega} \tag{34}$$

where ζ_0 can be viewed as a virtual origin.

Squire[49] further proposed inclusion of an apparent or eddy-viscosity parameter δ in Eq. (34) to account for effects of turbulent mixing on the diffusion rate of the tip vortex. This apparent viscosity coefficient δ must be a function of the vortex Reynolds number Γ_v/ν. Because, in practice, free lift-generated vortices dissipate their energy only slowly with time, the strength of the tip vortex is found to remain nominally constant,[21,44,50,51] and so it is reasonable to assume a constant value of δ. Representative values of δ for helicopter rotor vortices range from as low as 10 (at model scale) up to more than 1000 (at full scale), as verified through experimental correlation.[52] Note that, in general, it can be difficult to distinguish between changes in vortex core size resulting from viscous diffusion independently from changes resulting from filament straining because vortices convect in the flow behind an aircraft. Incorporation of Lamb-like vortex models, including a representation of viscous diffusion, generally give improved correlations between measured and predicted wake geometries and blade loads.[24,36]

Filament Straining

Because the Lagrangian markers are allowed to convect freely in the wake solution, the vortex filaments will be strained as adjacent markers move relative to each other. Because Helmholtz's third law requires the net strength of any vortex filament to remain constant, the product of the vorticity and its cross-sectional area must also remain constant. Stretching the vortex filament, therefore, increases its vorticity. For an axisymmetric vortex tube, this means that the area of the tube containing the vorticity must decrease, leading to an effective decrease in the size of the viscous core and a consequent change (increase) in the magnitude of the local induced velocity.

Such straining effects on filaments can be particularly significant in regions where adjacent filaments come into close proximity. For helicopter applications, such situations include the rollup of individual tip vortices into bundles on the advancing and retreating sides of the rotor disk, when the rotor is at high rates of descent where the wake may recirculate in the plane of the rotor, or in ground effect, where the presence of the ground on the rotor flow causes the wake to expand radially away from the rotor disk.[22] In many cases, filament straining effects are small compared to the effects of viscous diffusion, but the effects may not be negligible.

To analyze this straining effect with the vortex filament method, assume that $\boldsymbol{r}_{l-1}$ and $\boldsymbol{r}_l$ are the position vectors of two adjacent markers on a filament (Fig. 1). Because the filaments are straight segments, the line vector of the filament is $\boldsymbol{l} = \boldsymbol{r}_l - \boldsymbol{r}_{l-1}$. Therefore, the rate of change in filament length is given by

$$\frac{\mathrm{d}\boldsymbol{l}}{\mathrm{d}t} = \frac{\mathrm{d}(\boldsymbol{r}_l - \boldsymbol{r}_{l-1})}{\mathrm{d}t} = \boldsymbol{V}_l - \boldsymbol{V}_{l-1} \tag{35}$$

which means that the stretching of the filament can be determined in terms of the velocities of the Lagrangian markers. Because the filament method requires only the change in the magnitude of the vorticity of each straight filament and not the local vorticity for each fluid particle, then using the conservation of mass with the assumption of incompressible flow allows the change in the area over which the vorticity is distributed, that is, essentially the change in the viscous core radius, to be established using

$$\Delta r_c = r_c\left[1 - (\epsilon + 1)^{-\frac{1}{2}}\right] \tag{36}$$

where ϵ denotes the filament strain $\Delta l/l$. Although the exact treatment of the filament stretching problem is relatively complex and several different numerical implementations may be possible, the preceding approach includes straining effects on the vortex filaments to be represented along with their advection as a correction to the Biot–Savart induced velocities.

Far-Field Boundary Conditions

As already mentioned, the LHS of Eq. (5) is a wave equation with a characteristic speed equal to unity. The integration of this equation requires one initial condition in time, ψ, and one boundary condition in space, ζ. This is satisfied by attaching the vortex segments with appropriate initial strengths and viscous core structure (vorticity) to the blade at their origin at $\zeta = 0$. If the wake is subsequently truncated after some finite vortex age, for example, $\zeta_{\max}$, another boundary condition may be required. By the nature of the basic wave equation, the solution propagates along the characteristic lines with $\mathrm{d}\psi/\mathrm{d}\zeta = 1$ using information from previous steps, and no boundary condition is required at the truncation point. However, the induced velocity source term on the RHS of Eq. (5) certainly requires a boundary condition to be satisfied in the far wake.

To better understand the reason for such a boundary condition, the induced velocities can be written in a compact discrete form as

$$\boldsymbol{V}_{\text{ind}}(\psi_k, \zeta_l) = \sum_{i=1}^{\infty} \boldsymbol{V}(\psi_k, \zeta_l; \zeta_i) \tag{37}$$

where $\boldsymbol{V}(\psi_k, \zeta_l; \zeta_i)$ is the velocity induced by the ith vortex element extending from $\boldsymbol{r}(\psi_k, \zeta_{i-1})$ to $\boldsymbol{r}(\psi_k, \zeta_i)$ at a collocation point at $\boldsymbol{r}(\psi_k, \zeta_l)$. The net induced velocity is found by integrating along the length of each vortex filament extending from the blade tip to infinity. The induced velocity can be further divided into two parts as

$$\boldsymbol{V}_{\text{ind}}(\psi_k, \zeta_l) = \underbrace{\sum_{i=1}^{l} \boldsymbol{V}(\psi_k, \zeta_l; \zeta_i)}_{\text{younger vortex elements}} + \underbrace{\sum_{i=l}^{\infty} \boldsymbol{V}(\psi_k, \zeta_l; \zeta_i)}_{\text{older vortex elements}} \tag{38}$$

The force-free equilibrium position of each vortex segment collocation point located at $\boldsymbol{r}(\psi_k, \zeta_k)$ is given by an equilibrium between these two components of the induced velocity. If the wake is truncated at $\zeta_{\max}$, then only one part of the induced velocity is affected. Equation (38) can be rewritten to identify the velocity terms:

$$\boldsymbol{V}_{\text{ind}}(\psi_k, \zeta_l) = \underbrace{\sum_{i=1}^{l} \boldsymbol{V}(\psi_k, \zeta_l; \zeta_i)}_{\text{younger}} + \underbrace{\sum_{i=l}^{I_{\max}} \boldsymbol{V}(\psi_k, \zeta_l; \zeta_i)}_{\text{older}}$$

$$+ \underbrace{\sum_{i=I_{\max}}^{\infty} \boldsymbol{V}(\psi_k, \zeta_l; \zeta_i)}_{\text{wake truncation}} \tag{39}$$

When the point $\boldsymbol{r}(\psi_k, \zeta_l)$ is near the wake-truncation region, that is, ζ_l is close to $\zeta_{\max}$, the equilibrium position of the collocation point would be disturbed by the effects of truncation. Therefore, a far-wake boundary condition will be required to represent correctly the induced velocities there.

Note that in forward flight or climbing flight such a truncation boundary condition may not be required. This is because the relative errors introduced by truncation are smaller, that is,

$$\text{relative velocity errors from truncation} = \frac{\sum_{i=I_{\max}}^{\infty} \boldsymbol{V}(\psi_k, \zeta_l; \zeta_i)}{\boldsymbol{V}_{\text{freestream}} + \sum_{i=1}^{\infty} \boldsymbol{V}(\psi_k, \zeta_l; \zeta_i)} \tag{40}$$

where $\boldsymbol{V}_{\text{freestream}}$ can be viewed as an external velocity resulting from forward or climbing flight.

There are several approaches that have been used to define a boundary condition in the far wake of a hovering rotor. One approach is to prescribe an semi-infinite cylinder of vorticity extending to infinity. The induced velocity of a vortex cylinder can be calculated analytically (Refs. 53 and 54). Another variation is to use a stack of vortex rings (e.g., Refs. 30 and 55). However, these approaches are only applicable to hovering flight. Another parsimonious approach would be to use prescribed wake geometry for the wake beyond a specified number of free turns (e.g., Ref. 15). Such approaches are suitable for many quasi-steady flight conditions, but any prescribed boundary conditions are generally unsuitable for time-accurate wake calculations.

A more preferable approach in dealing with wake truncation is to use a velocity field extrapolation technique. Figure 4 shows a schematic that helps explain the idea of velocity field extrapolation. The free-vortex solution is first solved up to N wake turns. Additional wake turns are then specified as a boundary condition. For sufficiently large N, it is reasonable to assume that the induced velocity field from the $N+1$th turn is nearly the same as that of the Nth turn. To extrapolate the induced velocity field, the free-vortex wake is calculated up to, for example, a wake age of ζ_F. For collocation points older than ζ_F, the velocity field is not explicitly calculated, but extrapolated along the characteristic, $\mathrm{d}\psi/\mathrm{d}\zeta = 1$. Therefore, this gives

$$\boldsymbol{V}(\psi_k, \zeta_i) - \boldsymbol{V}(\psi_k - \Delta\psi, \zeta_i - \Delta\zeta)$$

$$= \boldsymbol{V}(\psi_k, \zeta_i - 2\pi) - \boldsymbol{V}(\psi_k - \Delta\psi, \zeta_i - 2\pi - \Delta\zeta) \tag{41}$$

where an equal discretization ($\Delta\psi = \Delta\zeta$) has been assumed. Therefore, the velocity field for the boundary condition turns of the rotor wake can then be calculated.

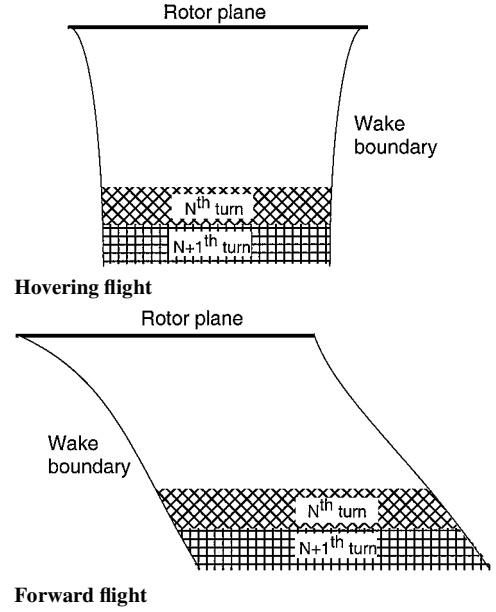

Fig. 4 Schematic of the far-field extrapolation boundary condition for the rotor wake.

Wake Solution Acceleration Algorithms

Because of the large number of field markers in a typical free-vortex wake problem, the integration schemes can be relatively costly for routine use, especially when coupled to a rotor performance or other iterative design analysis. Some acceleration methods have used simplified wake models based on ring vortices, limited wake distortion degrees of freedom (e.g., Ref. 16), analytical approximations for curved vortex segments (e.g., Ref. 11) or exploitation of parallel computing capabilities (e.g., Ref. 56). The most common approach, however, is simply to reduce the number of induced velocity field calculations. This can be done by updating the induced velocities less frequently by using fewer vortex elements in the discretized wake, by subdividing the wake into near-field and far-field regions of weak and strong influence, or by more elegant near-field/far-field matching procedures (e.g., Ref. 27). However, although successful in decreasing execution times, resulting higher-order velocity field errors associated with the approximations may still undermine the accuracy of the wake predictions. Linear interpolation of the positions of the wake markers simply to effect a larger number of points, such as discussed in Ref. 57, does not improve the net accuracy of the wake solution.

Methods for using an interpolated velocity field in free-vortex wake calculations was introduced by Bagai and Leishman.[58] The underlying goal was to perform fewer explicit induced velocity calculations using the Biot–Savart law, while retaining the accuracy and fidelity of the wake solutions. For equal discretization ($\Delta\psi = \Delta\zeta$) with $N_\psi = 2\pi/\Delta\psi$ azimuthal steps per rotor revolution, the number of vortex segments in each wake turn is $N_\zeta = N_\psi = N$. Therefore, the number of Biot–Savart calculations required is $N_b N_\psi N_\zeta^2 = N_b N^3$. Velocity field interpolation reduces the effective number of Biot–Savart calculations by using both "free" and "pseudofree" Lagrangian markers. For the case where $\Delta\zeta > \Delta\psi$, the induced velocities are calculated explicitly only at the free Lagrangian markers spaced at $\Delta\zeta$ and by linear interpolation of the velocity field at the pseudofree markers. Therefore, the number of Biot–Savart evaluations is decreased by a factor corresponding to the ratio of the discretization $\Delta\zeta/\Delta\psi$. For example, with $\Delta\zeta = 2\Delta\psi$, the number of Biot–Savart calculations is reduced by a factor of four to $(N_b N^3)/4$. In a time-marching approach, this interpolation scheme is applied after each time step, whereas when using the relaxation algorithm, the interpolation is applied over the entire domain with a wake interation.

In addition to the overall lower cost of a relaxation algorithm, another advantage is that azimuthal interpolation can be used where

$\Delta\psi > \Delta\zeta$. The basic approach is similar to that described for vortex filament interpolation, the difference being that the interpolation is performed at a constant vortex age along the blade azimuth. This results in a computational saving of a factor of $\Delta\psi/\Delta\zeta$ of the number of Biot–Savart velocity evaluation points. However, the total number of wake markers remains unchanged. For example, with $\Delta\psi = 2\Delta\zeta$ times, the number of Biot–Savart calculations is reduced by half to $(N_b N^3)/2$. The blade attachment boundary condition, that is, the first Lagrangian marker, needs special treatment in this case. These values may be obtained by interpolating the blade flapping angles with respect to ψ or, alternatively, by exactly solving for a periodic blade flapping solution at all blade azimuthal locations. Azimuthal interpolation is a redundant acceleration technique for the time-marching approach because it is always necessary to use small time (azimuthal) steps to preserve accuracy in time.

Results and Discussion

Rotor Wake Geometry

The validity of any wake model can only be determined through comprehensive correlation studies with experimental measurements. Figures 5 and 6 show an example of the top (plan) and side

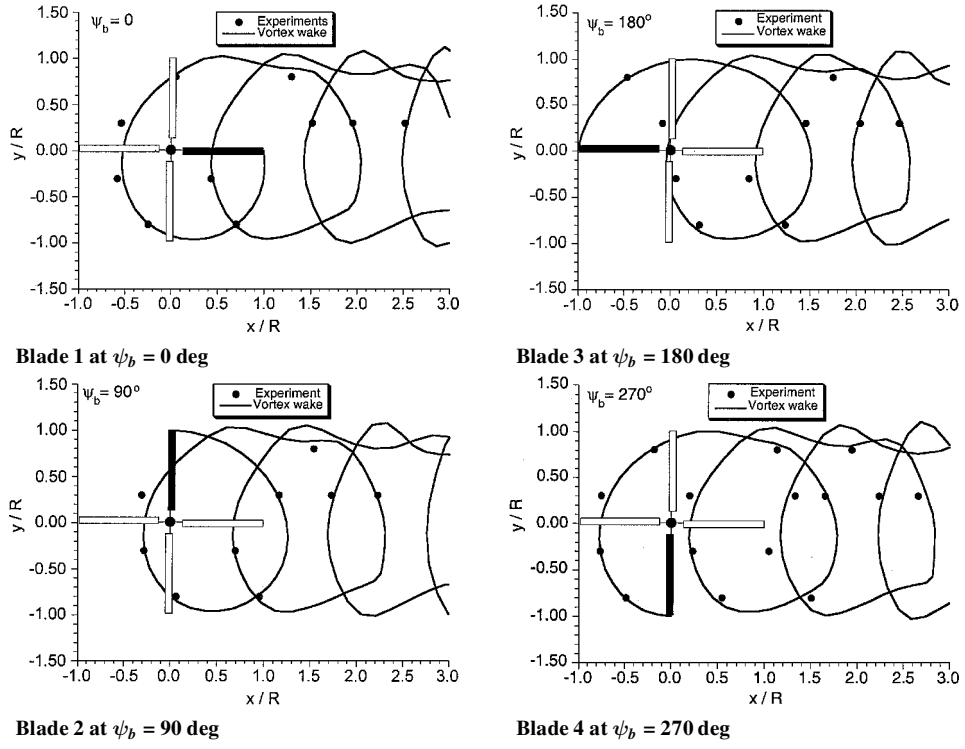

Blade 1 at ψ_b = 0 deg **Blade 3 at ψ_b = 180 deg**

Blade 2 at ψ_b = 90 deg **Blade 4 at ψ_b = 270 deg**

Fig. 5 Predicted top views of the rotor tip vortex trajectories compared with flow visualization measurements; results for each blade shown separately.

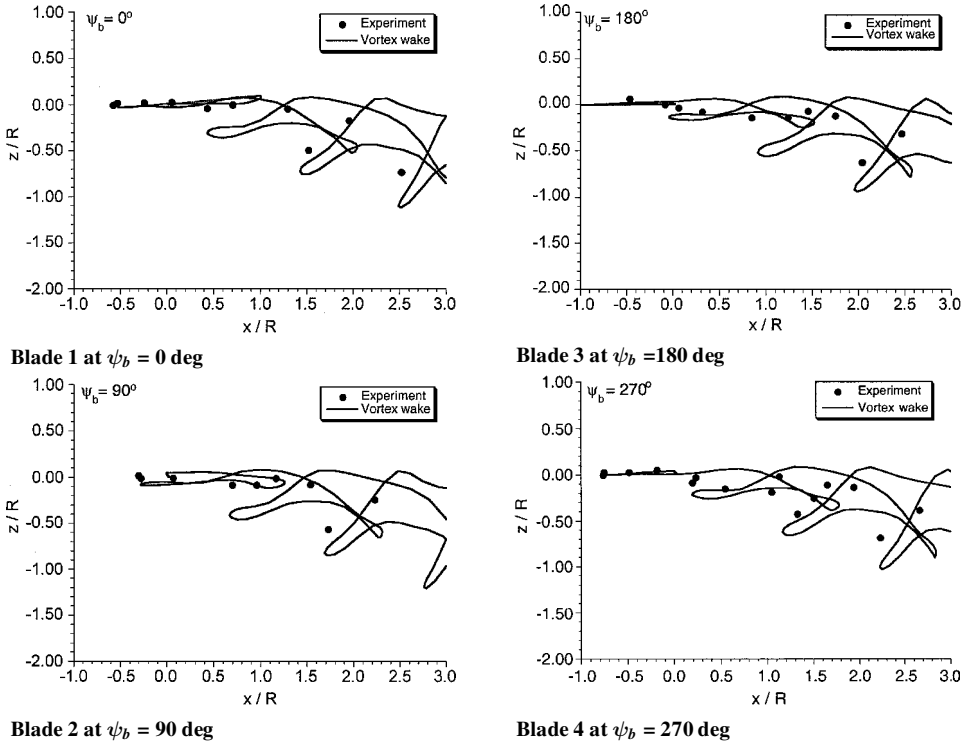

Blade 1 at ψ_b = 0 deg **Blade 3 at ψ_b =180 deg**

Blade 2 at ψ_b = 90 deg **Blade 4 at ψ_b = 270 deg**

Fig. 6 Predicted side views of the rotor tip vortex trajectories compared with flow visualization measurements; results for each blade shown separately.

view of the rotor wake generated by a four-bladed rotor operating in forward flight. The results are for an advance ratio of $\mu = 0.15$, a thrust coefficient of $C_T = 0.008$, and the rotor shaft tilted forward by 3 deg. The trajectories of the tip vortices from each blade are plotted separately for clarity. The predicted trajectories are compared with measured tip vortex displacements from Ref. 59, which were determined using smoke seeding with a strobed laser sheet visualization technique.

Notice that the free-wake predictions show good overall agreement with the experimental results. When viewed from above (Fig. 5) the tip vortex trajectories trace out essentially epicycloidal trajectories, with only slight in-plane distortions. Only at the lateral edges of the wake is some distortion notable, which is because of the rollup between individual vortices and the formation of vortex bundles. The small radius of curvature of the wake filaments in this region requires closely spaced markers to capture the rollup correctly. Although the streamwise displacements closely resemble an epicycloidal form, the vertical displacements of the tip vortices undergo much larger distortions, as shown in Fig. 6. Notice that the tip vortices remain very close to the tip-path plane at the front of the rotor disk, but convect quickly downward as they reach the rear of the disk. In most cases, there are many close encounters between the blades and the tip vortices, which are called blade–vortex interactions (BVIs). Accurate prediction of the unsteady airloads and noise associated with BVI demands that the wake be modeled to a good level of accuracy.

Grid Sensitivity

To be physically meaningful, the free-vortex wake solution should be insensitive to grid discretization, a result that can only be verified by numerical experiments. Although the exact (mathematical) solution for the wake problem is indeterminate, a numerical solution with a fine grid discretization can be considered as the exact solution for the purpose of estimating the order of accuracy. Also, because both stability and consistency are necessary for solution convergence, numerical experiments can also verify the stability of the solution algorithm.

Representative results are shown in Fig. 7 for a four-bladed rotor whose geometry and operating conditions correspond to the experiments of Ref. 59, as already described. These results were computed using the time-marching PC2B algorithm. The top (plan) and side views of the rotor wake geometry are shown in Figs. 7a and 7b for different levels of discretization. Only the tip vortex from a reference blade at $\psi_b = 0$ deg is shown in this case to preserve clarity. Notice that only the solution with the coarser discretization of $\Delta\psi = \Delta\zeta = 20$ deg shows significant differences from the other solutions; the solutions corresponding to $\Delta\psi \leq 10$ deg are much closer. As shown in Fig. 7c, the numerical errors relative to the $\Delta\psi = 2.5$ deg solution exhibited good second-order accuracy. This type of accuracy check verifies that not only is the selected algorithm stable but also that the final numerical solution is stable, consistent, and, therefore, properly convergent. Similar results were obtained using the relaxation approach.

Accelerated Wake Solutions

An example of the wake geometry obtained using linear velocity field interpolation with a time-marching algorithm is shown in Fig. 8 for a rotor operating in hovering flight. The axial wake displacements are shown in Fig. 8a as a function of vortex age for two equal discretization levels of $\Delta\psi = \Delta\zeta = 2.5$ and 5 deg along with a solution obtained using linear velocity field interpolation for $\Delta\psi = 2.5$ and $\Delta\zeta = 5$ deg. The solution using interpolation closely resembles the solution obtained using finer resolution, that is, $\Delta\zeta = \Delta\psi = 2.5$ deg. The convergence trends obtained using the interpolation technique with $\Delta\zeta = 2\Delta\psi$ are shown in Fig. 8b. The velocity field interpolation should yield a second-order accuracy in the tip vortex locations, which is confirmed by the quadratically decreasing convergence trend shown. Note that for any given discretization $\Delta\psi$, the errors using interpolation are larger than the corresponding errors for the baseline equal discretization. However,

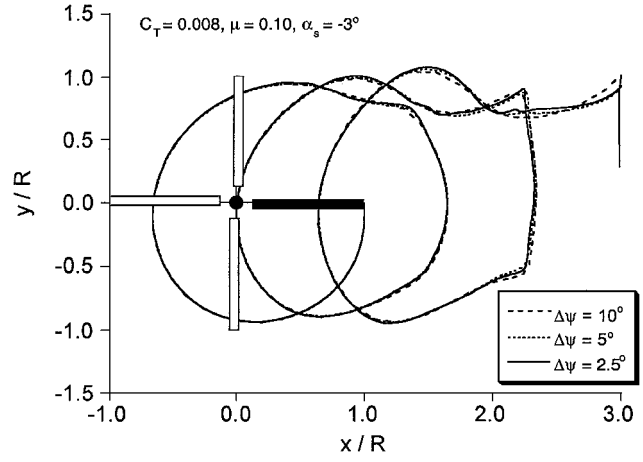

a) Top view of wake geometry

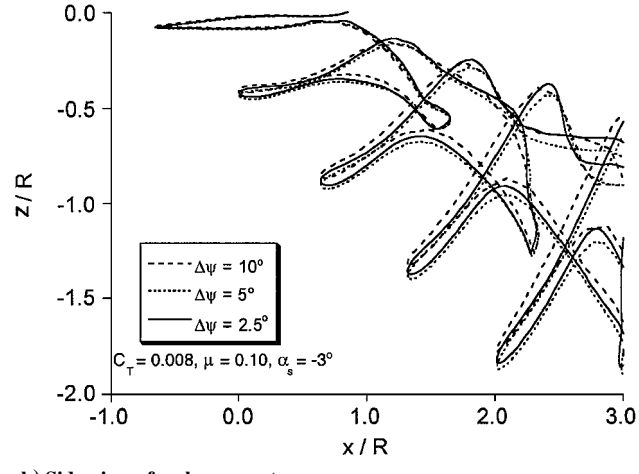

b) Side view of wake geometry

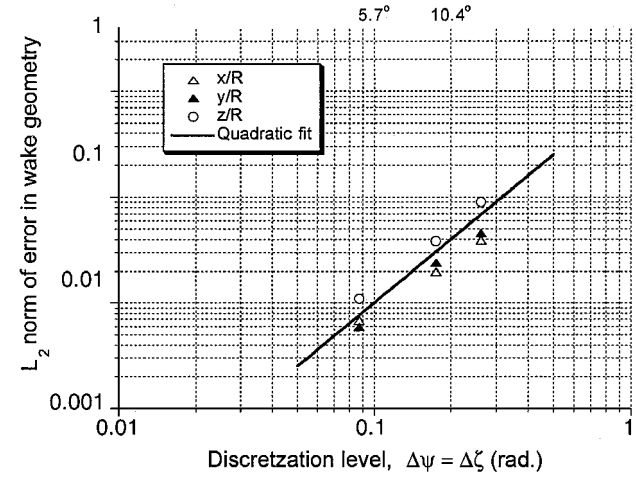

c) Convergence trend

Fig. 7 Numerical errors with increasing grid discretization as a function of discretization to verify convergence of the PC2B algorithm; forward flight solution, forward shaft tilt angle of = − 3 deg, C_T = 0.008, and μ = 0.1.

the errors are significantly smaller than the corresponding errors for the baseline solution with $\Delta\psi = \Delta\zeta$, that is, the errors in interpolated solution with $\Delta\psi = 5$ deg and $\Delta\zeta = 10$ deg are smaller than those for the baseline solution with $\Delta\psi = \Delta\zeta = 10$ deg. Therefore, velocity field interpolation is one technique that can be used to obtain accurate wake solutions without the computational overhead of a finer discretization. Similar results were again obtained using the relaxation method.

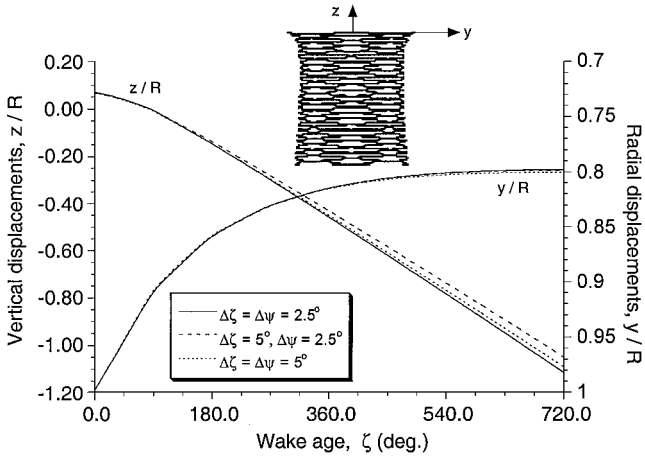

a) Axial and radial tip vortex displacements

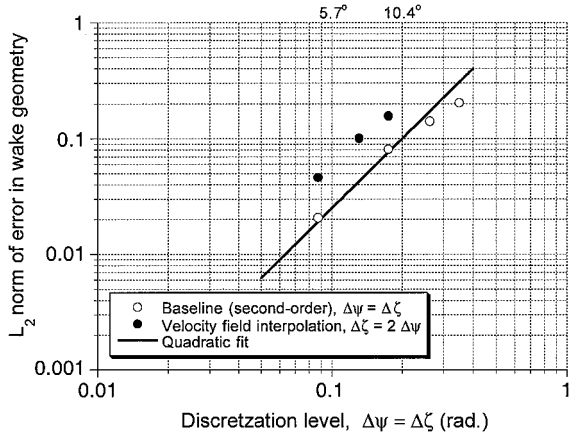

b) Wake convergence trend

Fig. 8 Velocity field interpolation used in the free-vortex wake solution with $\Delta\zeta = 2\Delta\psi$ to reduce computational expense; hovering wake solution, four-bladed rotor, and $C_T = 0.008$.

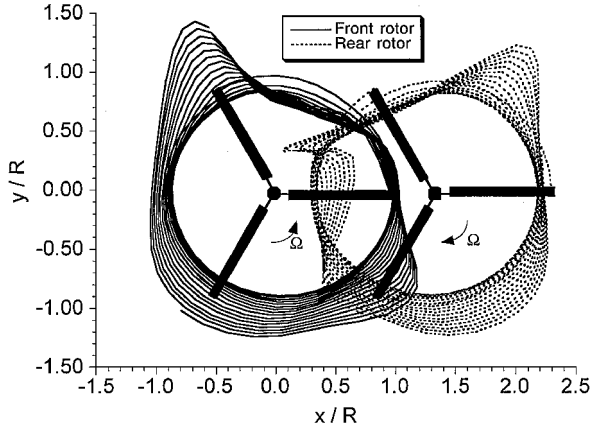

a) Top view

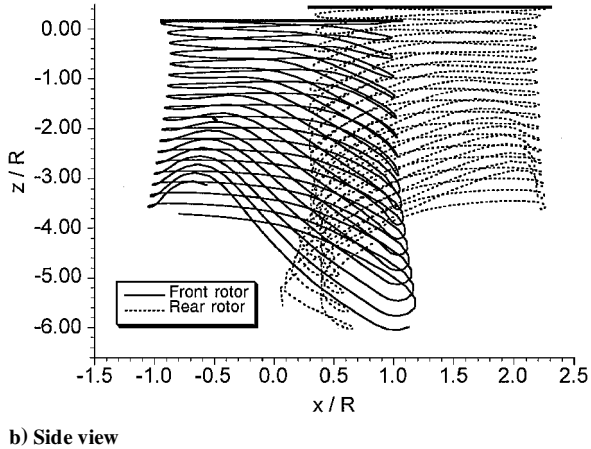

b) Side view

Fig. 9 Representative predicted wake geometries for a tandem, overlapping rotor configuration operating in hover.

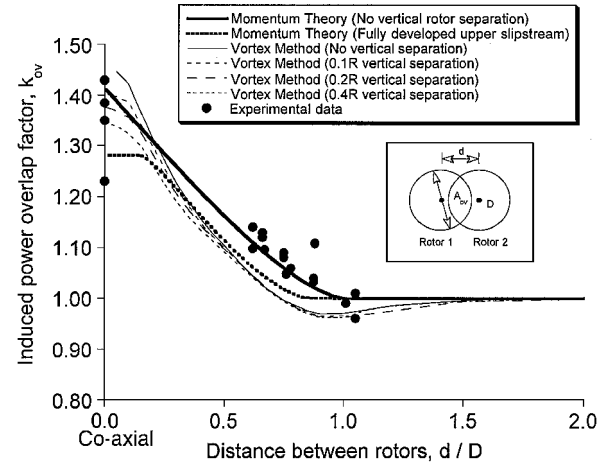

Fig. 10 Induced power overlap factor for tandem rotors in hover as a function of separation distance between rotors; experimental results from Refs. 60 and 63 (Vol. 2, Chap. 5).

Multirotor Configurations

Measurements and prediction of the performance of multirotor configurations have received some attention in the literature[60–63] and mainly use an extension of the simple momentum theory. The free-vortex wake methodology can be extended to model multiple rotor configurations such as coaxial rotors, overlapping tandems, or side-by-side configurations such as tilt rotors. A tandem overlapping rotor configuration is one of the most interesting and challenging because there are powerful interactions between the two developing rotor wakes, and the performance of the rotors may be quite different compared to two isolated rotors.

The free-vortex wake analysis of multirotor wake interference has been considered in Refs. 64 and 65. An example of the wake-on-wake effects produced by a tandem overlapping design is shown in Fig. 9, which is for hovering flight with the rotors both operating at a thrust coefficient of $C_T = 0.008$. Significant interactions between the two rotor wakes are clearly evident in the rotor overlap region along the edges between the two rotor wakes (Fig. 9a), although the top view of the wakes (Fig. 9b) shows that these distortions are not just confined to the overlap region. Notice the much higher axial convection velocity of the filaments that are trailed into the overlap region.

The performance of overlapping rotors is usually approached semi-empirically.[63] A momentum theory analysis of tandem rotors can be used as a reference for this problem, which is based on the idea of overlapping areas of the rotor disks. The momentum theory results are shown in Fig. 10 in terms of an overlap induced power factor κ_{ov} as a function of rotor separation, along with free-vortex wake predictions for increasing rotor separation distance and different vertical spacing between the rotors. The free-vortex results used a four-bladed rotor, with linear blade twist. Note that, because momentum theory is based on uniform inflow and noninteracting overlap areas, no interference effects are predicted, that is, $\kappa_{ov} = 0$, for $d/R \geq 1$ for no vertical rotor spacing or for $d/D > 0.854$ where the lower rotor operates in the fully developed slipstream of the upper rotor. In the latter case, the wakes remain fully overlapped if $d/D < 0.14645$, and so the interference factor κ_{ov} remains constant over this region.

Notice that the free-wake analysis results shown in Fig. 10 suggest that there is a range of values of d/D for which there is a favorable interference between the two rotors giving slightly lower induced power requirements, that is, $\kappa_{ov} < 1$. This is because the vortical rotor wakes interact with each other resulting in wake distortion effects, which, for some conditions, tend to slightly decrease the induced power requirements. This implies that helicopter configurations with closely spaced multiple rotors can potentially be aerodynamically more efficient than a single rotor with the same disk loading.

Ground Effect

The performance of a helicopter rotor may be affected significantly by the presence of a solid boundary such as the ground, which may constrain the development of the rotor wake. This phenomenon, called ground effect, is apparent in actual flight operations as well as during wind-tunnel testing of rotors. For in-ground effect (IGE) operations in hover and at very low forward speeds, there is usually a favorable effect in that the rotor power required to produce a given thrust is lower than the power required out-of-ground effect (OGE).

The vortex wake methodology can be applied to study the ground effect phenomenon by one of two approaches. First, the method of images can be used. In this approach, a second rotor with the identical aerodynamic loading and wake geometry as the real rotor is placed in such a way as to create an image plane of symmetry between the two. Second, a surface singularity method can be used where the boundary condition of flow tangency is explicitly applied on the ground surface, and the induced effects of these surface singularities are accounted for by modifying the net velocity field. See Refs. 65–68 for applications of the vortex wake method to ground effect problems.

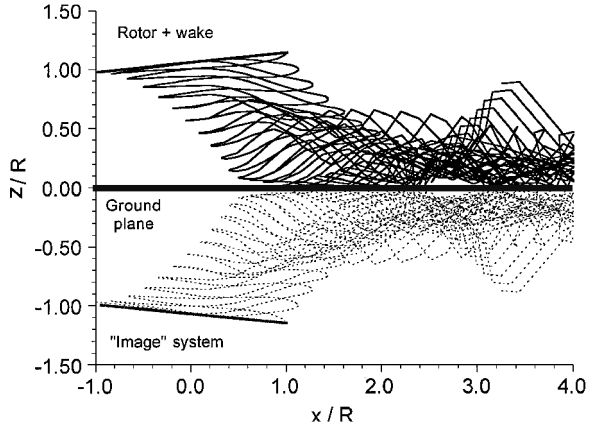

a) Side view

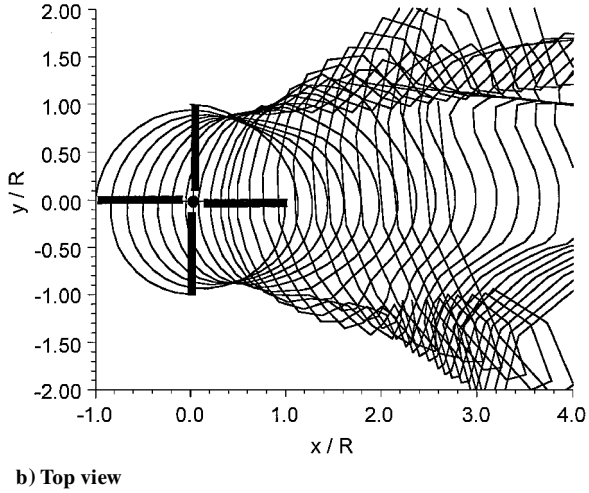

b) Top view

Fig. 11 Example of a predicted wake geometry using method of images to simulate ground effect, four-bladed rotor, C_T = 0.008, forward shaft tilt α_s = 10 deg.

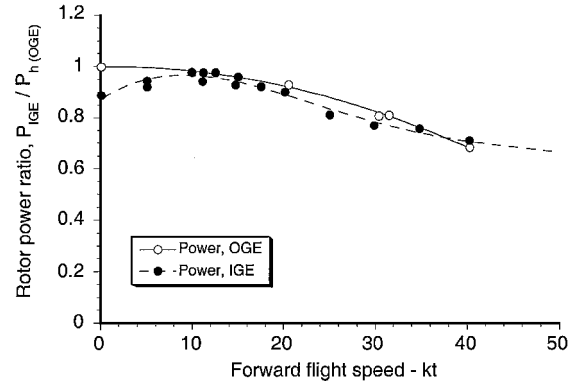

Representative measurements from Sheridan and Wiesner (see Ref. 69)

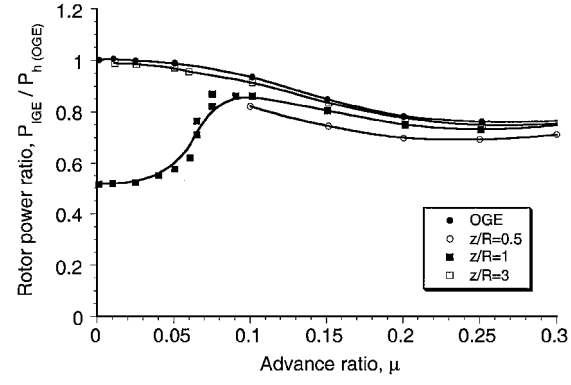

Free-vortex wake scheme

Fig. 12 Rotor power requirements IGE relative to hover power OGE as a function of rotor height off the ground and forward flight speed.

A representative prediction of the rotor wake when influenced by the ground is shown in Fig. 11 for a four-bladed rotor operating in forward flight. The method of images has been used, where real rotor is located $1.5R$ above the ground plane, with the mirror-image rotor being located $1.5R$ below the ground plane. This mirror-image rotor rotates in a counter direction to the real rotor, and its thrust is directed vertically downward. The side view of the resulting rotor wake structure, which is shown in Fig. 11a, suggests significant wake distortions in the region when the wake approaches the ground plane. These distortions change the velocity field and also influence the development of the wake closer to the rotor and can possibly affect the rotor performance. Of significance in this case is the large stretching of the vortex filaments in the far wake rollup region, suggesting the need for a higher resolution representation of the wake for these types of problem.

The top view of the rotor wake is shown in Fig. 11b and vividly illustrates the distortion to the rotor wake resulting from the influence of the ground. Notice that ground effect causes the rolled-up trailing vortex bundles to move laterally away from the the edges of the rotor (c.f. Fig. 5), in effect resulting in an apparent increase in the effective aspect ratio of the rotor. In hovering flight and for some range of advance ratios, this gives a very favorable decrease of the induced power required to generate a given thrust (Fig. 12). Notice, however, that there can be a rapid increase in power required as the helicopter transitions from hovering flight IGE into forward flight IGE relative to the corresponding power required OGE, which has been documented experimentally.[69] Generally the effects of the ground are found to be small when the rotor is more than $3R$ above the ground plane and/or for advance ratios greater than 0.10.

Maneuvering Flight

The ability to predict the aerodynamic response of a rotor under maneuvering flight conditions is fundamental to the improved

design of modern military helicopters. Many real maneuvers that helicopters routinely perform, such as turns, involve small angular rates compared to the rotor rotational frequency; typical rates are $p/\Omega, q/\Omega \leq 0.025$. Therefore, the computational benefits of a relaxation-based vortex wake model can be used to represent quasi-steady maneuvering flight aerodynamics, provided that any transient effects introduced into the wake resulting from the maneuver are of a relatively short time period. However, a time-accurate wake model will usually be necessary to represent properly high-rate maneuvers, such as transient pull-ups and wind-up turns, and to investigate the time evolution of the rotor wake and rotor response.

General maneuvers comprise combinations of translational and angular motions and especially involve rates and accelerations. The effects can be modeled using an additional contribution to the local velocity vector on the RHS of Eq. (14). Angular rates about the roll, pitch, and yaw axes contribute heavily to the wake distortions produced during maneuvers. The equivalent external velocity resulting from rate-type maneuvers can be determined from a cross product of the maneuver rate vector (p, q, r) and the position vector of a wake element $\boldsymbol{r}$ using

$$\begin{aligned} \boldsymbol{V}_{\text{ex}} &= -(p, q, r) \times (x, y, z) \\ &= -(qz - ry)\hat{i} + (pz - rx)\hat{j} + (qx - py)\hat{k} \end{aligned} \tag{42}$$

The first term in Eq. (42), which is the x or streamwise component of the velocity resulting from a pitch rate q and/or a yaw rate r, essentially produces a skewing distortion of the wake. The second term, which is the y or lateral component of the velocity resulting from a roll rate p and/or a yaw rate r, produces a skewing in the lateral direction. The third $(qx - py)$ term in Eq. (42) results in an asymmetric axial stretching distortion of the wake, which appears like a wake curvature. Figure 13 shows representative wake geometries for a four-bladed rotor opering in forward flight.

These maneuver-induced wake distortions result in changes to the rotor-induced velocities, and, hence, to the rotor airloads and blade flapping response, and are responsible, at least in part, for difficulties in predicting the so-called off-axis response of helicopters during certain maneuvers.[70–73] This off-axis effect can manifest as a powerful initial pitch response to pilot roll input commands and so is an undesirable flight characteristic. The relative effects of maneuver-induced wake distortion on the induced inflow distribution will be a function of advance ratio, as well as for positive and negative pitch and roll rates mainly because of the highly nonaxisymmetric nature of the wake in forward flight.[74]

For example, Fig. 14a shows the component of the on-axis (longitudinal) inflow gradient perturbation resulting from a positive (nose-up) quasi-steady pitch rate motion as a function of advance ratio for a four-bladed articulated rotor. The kinematic inflow gradient produced by the maneuver, which is simply $-qx/\lambda_0$, where λ_0 is the mean or average inflow, shows a negative perturbation for positive pitching rate. This perturbation slowly increases in magnitude, which is because of the initial decrease in mean rotor inflow with increasing advance ratio. Notice that at low advance ratios, including hover, the free-vortex wake predicts maneuver-induced wake distortions that change the inflow perturbation in a sense opposite to the kinematic effects. It is also significant that at $\mu \approx 0.1$ the trend reverses and the maneuver-induced wake distortion results in an inflow gradient

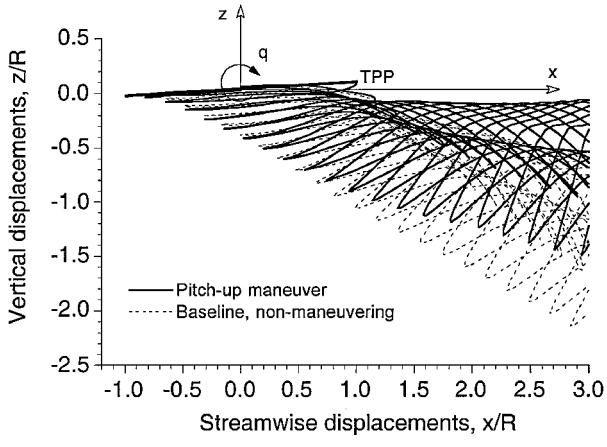

Side view of wake for nose-up pitch rate with $q/\Omega = 0.012$

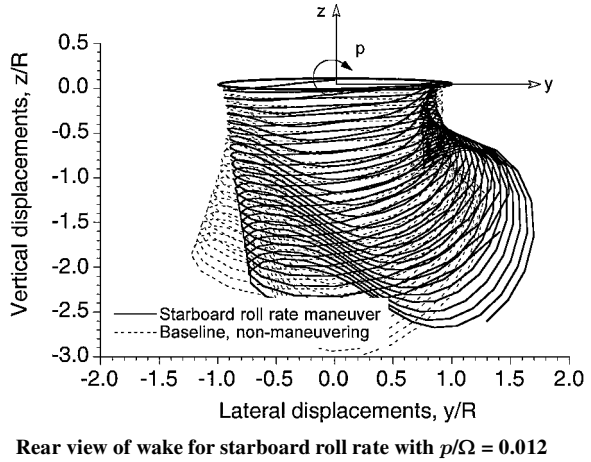

Rear view of wake for starboard roll rate with $p/\Omega = 0.012$

Fig. 13 Representative predicted wake geometries for a four-bladed rotor opering in forward flight at $\mu = 0.10$ and $C_T = 0.008$ during a simulated maneuvers.

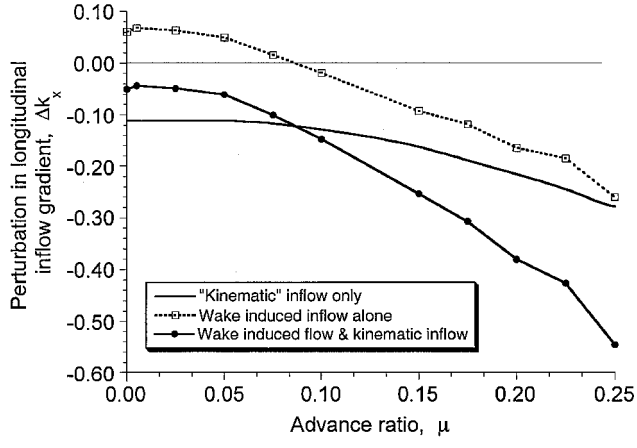

a) Induced inflow perturbations

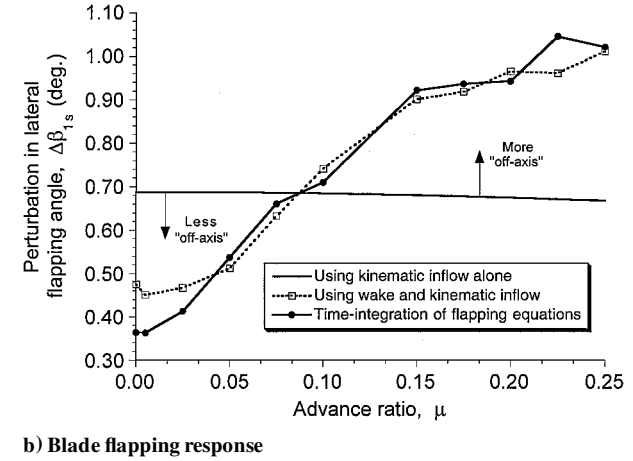

b) Blade flapping response

Fig. 14 Induced inflow perturbations and corresponding blade flapping response for a four-bladed rotor resulting from an imposed pitch rate of $q/\Omega = 0.012$ as a function of advance ratio.

perturbation that is now in the same sense as the kinematic inflow perturbation.

The corresponding change in lateral blade flapping response $\Delta\beta_{1s}$ for this nose-up pitch rate problem is shown in Fig. 14b. The β_{1s} term determines the lateral tilt of the rotor disk, and so is a measure of the tendency for the rotor to roll, that is, an off-axis response in this case. The blade flapping predicted using the kinematic inflow gradients alone was found to be nominally constant with advance ratio. However, the solution obtained by using the free-vortex wake method along with simultaneous time integration of the blade flapping equations showed that in hover and at low advance ratios the blade flapping was smaller than would be predicted without including the maneuver-induced wake distortions, at least for this rotor. At higher advance ratios, the wake distortion effects produced inflow gradients similar in magnitude to the kinematic gradients, potentially resulting in a more pronounced off-axis blade flapping response. Although this result does not explain the significant off-axis blade flapping found during flight tests with some helicopters, the rotor wake dynamics clearly plays a significant role in the maneuver problem.[73]

Vortex Ring State

Another challenging application for vortex wake models is to predict the aerodynamic conditions at the rotor during descending flight. In low-speed descents, the flow at the rotor can be significantly unsteady (aperiodic), with the maximum fluctuations in the rotor response occurring near the vortex ring state (VRS).[75–78] The VRS phenomenon usually manifests itself as a substantial increase in the required power for equilibrium flight because it is necessary to overcome the additional aerodynamic losses as the rotor descends into its own wake. As a consequence, the VRS condition is often referred to by pilots as "settling with power." More important, however, the unsteady flow obtained during transition into and through the VRS may result in highly fluctuating blade airloads leading to considerable blade flapping and poor control effectiveness. Although sustained operation in the VRS is undesirable, transition through the VRS may be required to reach autorotative conditions, and so prediction of the airloads and rotor performance in the VRS is of particular interest to the rotor aerodynamicist.

Whereas simple momentum theory has been used to analyze this VRS problem,[79,80] it is strictly invalid in the VRS because of the ambiguity in defining a single flow direction and a well-defined slipstream boundary that encompasses only the rotor disk area (e.g., Ref. 1). Also, periodic (relaxation) vortex wake models fail to predict the rotor behavior near the VRS because of the inherent aperiodicity of the flow, and a time-accurate wake model must be used.

To illustrate the transient, unsteady nature of the flow state during operation in the VRS, Fig. 15 shows the free-vortex wake predictions of the thrust and power, as well as the blade flapping (coning) angle, for a rotor starting from hover and rapidly accelerating into vertical descent. Further details of the approach are given in Refs. 81 and 82. The collective pitch of the rotor is reduced compared to that required for hovering flight, but no attempt was made here to trim the rotor during this transient flow problem. Note that the results in Fig. 15 have been normalized with respect to the equilibrium values in hovering flight. As the rotor first begins to descend, only small oscillations in rotor thrust and blade flapping are observed. However, during the transition into the VRS as the rotor descends into its own wake, the rotor performance and flapping responses show significant unsteadiness. During this transition process, the rotor begins to extract power from the surrounding air, and the flow surrounding the rotor becomes highly aperiodic. As the descent rate increases further, the rotor begins to transition out of VRS and enters into the windmill brake state, where autorotation is achieved, as shown by the near-zero power consumption in Fig. 15c. At these higher rates of descent, the flow again becomes mostly periodic.

Figure 16 shows the corresponding predictions of the rotor wake boundary during the transition from hover through the VRS into steady descending descent. At low descent rates, as shown by

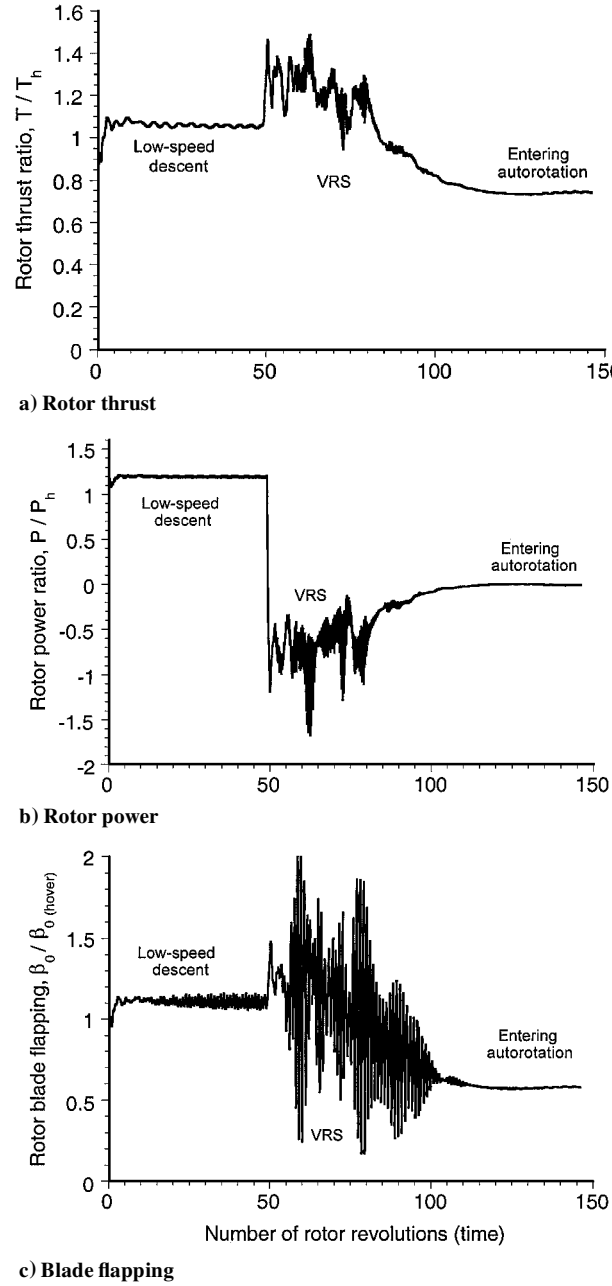

Fig. 15 Representative time-history predictions of rotor thrust, rotor power, and blade flapping during transition from hover through the VRS to axial descending flight.

Fig. 16b, the rotor wake begins to move up into the plane of the rotor disk. As shown in Fig. 16c, for higher rates of descent, the wake contracts and moves up through the rotor disk, and this corresponds to the beginning of the fluctuations shown in Fig. 15. As the descent rate increases further and exceeds a descent velocity that is of the same magnitude but of opposite direction to the average induced velocity through the rotor, that is, $V_c + v_i < 0$, the wake rolls up around and through the rotor disk, with most of the discrete blade tip vortices trailed into the wake being bundled into the plane of the rotor see (Fig. 16d). This is symptomatic of the VRS, and Fig. 15 has already shown that it is accompanied by the highest oscillations in blade airloads and rotor flapping response. If the descent rate continues to increase so that $V_c + v_i \ll 0$, the rotor enters into the turbulent wake state, which is a flow state with relatively lower fluctuating loads, but it is still a relatively unsteady condition. At the highest descent rates, the rotor begins to enter the windmill brake state, and the wake attains a mostly periodic (axisymmetric) wake structure.

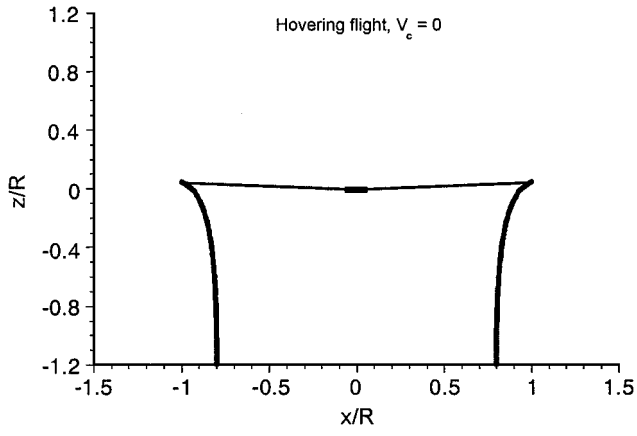

a) Hovering flight

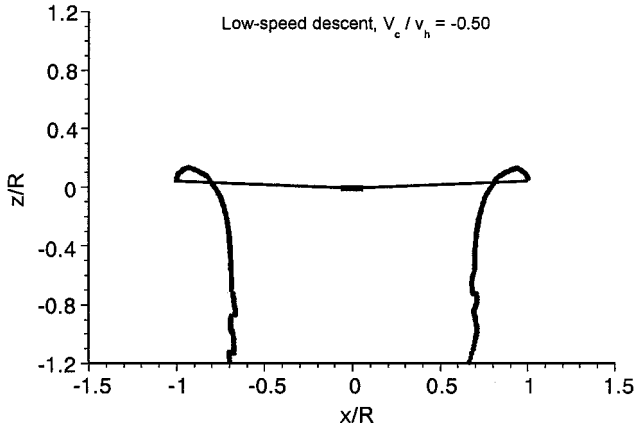

b) Low descent rate

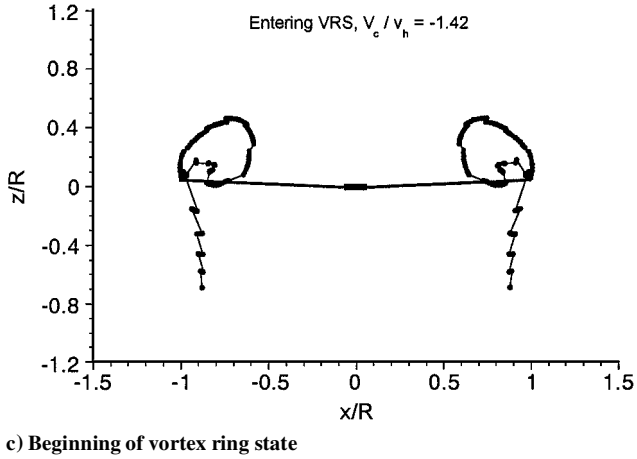

c) Beginning of vortex ring state

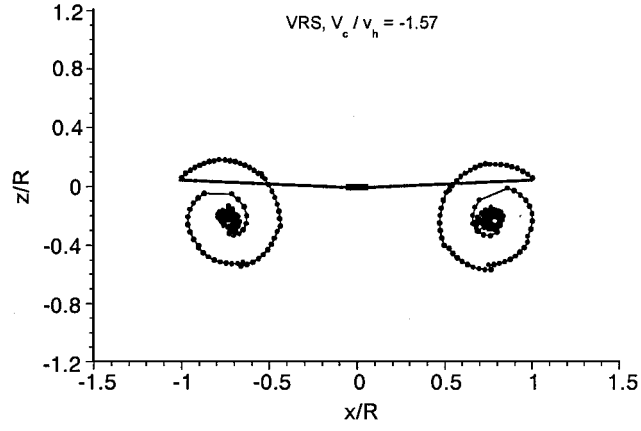

d) VRS

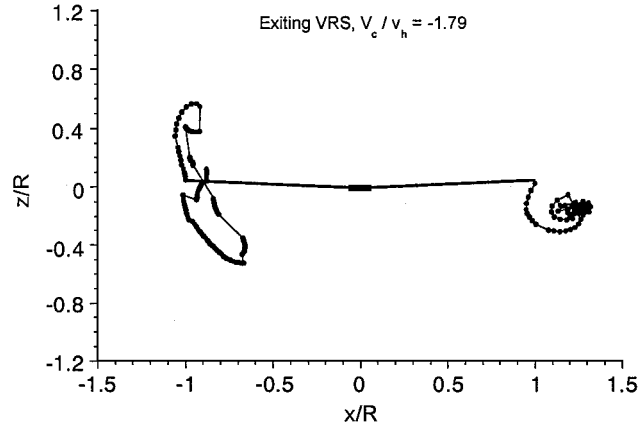

e) Larger descent rate approaching turbulent wake state

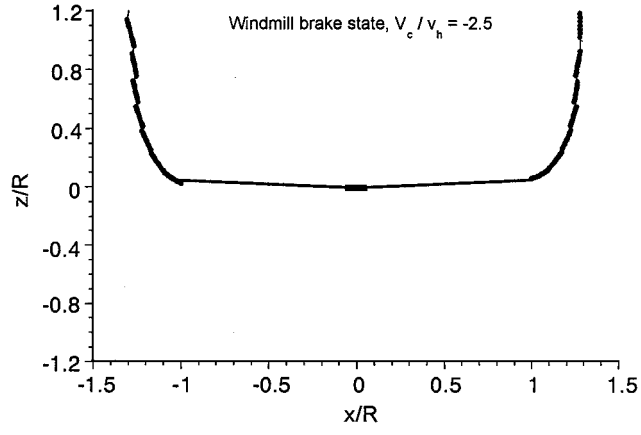

f) Windmill brake state

Fig. 16 Rotor wake boundary as viewed in a plane normal to the rotor disk during transition from hover through the VRS into axial descending flight.

Figure 17 shows the complete induced velocity curve for a rotor in axial (vertical) flight. The flight regime of interest for the VRS is for $-2 \leq V_c/v_h \leq 0$, where momentum-based theories are strictly invalid because of the reasons already mentioned. Experimental results are shown along with numerical predictions using the time-accurate free-vortex wake model. The induced velocity was determined from an estimate of the induced power, which was estimated from the measurements of total shaft power by assuming that the profile power P_0 is a function of the thrust alone and does not depend on the axial velocity. Therefore, the profile power was estimated from the measurements in hovering flight with the induced power being approximated by the simple momentum theory. The induced power in axial flight was then calculated by subtracting the profile power and loss of potential energy per unit time from the total measured power using $C_{P_i} = C_P - C_{P_0} - \lambda_c C_T$, from which the induced velocity ratio can be obtained from $\lambda_i = C_{P_i}/C_T$. Notice from Fig. 17 that at low descent rates both the experimental results and the predictions generally follow the nonphysical branch of the momentum theory solution. However, in this region, the averaged induced velocity is considerably higher than that predicted based by momentum theory alone. This is because under these conditions the rotor operates inside its own vortical wake, so that to produce the same thrust the rotor must consume more induced power. The free-vortex results were found to be in good agreement with the measurements, including operations deeply inside the VRS. In particular, note that the magnitude of the fluctuations are well predicted in this highly nonsteady flow state.

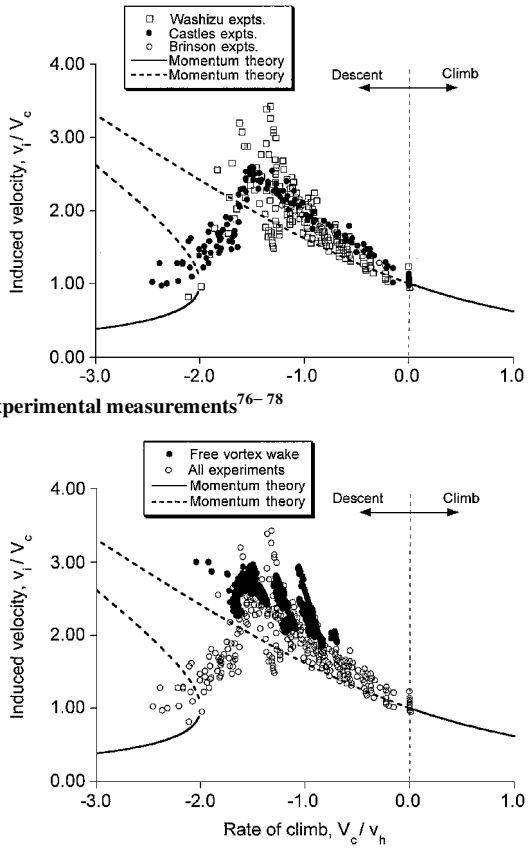

Fig. 17 Complete induced velocity curve for a rotor in vertical descending flight through the vortex ring state.

Conclusions

Over the last 30 years, there has been good progress, by means of a variety of computational methods, in representing the physics of helicopter rotor wakes. However, the complete understanding and rigorous numerical modeling of the problem still remains one of the greatest challenges facing rotor analysts. This paper has reviewed the theoretical basis and numerical implementation of one class of free-vortex filament methods, which have proven to be robust and flexible numerical methods that can be applied to the prediction and analysis of helicopter rotor wakes.

In vortex filament methods, the rotor wake is discretized into vortex filaments defined by a series of Lagrangian markers. It has been shown how the governing equation for the free-vortex wake problem can be reduced to a system of ODEs that describe the convection of these markers through the flow. Finite difference approximations to the governing equations have been described, along with a discussion of numerical solution algorithms using both relaxation and time-marching techniques. It is argued how the careful consideration of consistency, numerical stability, and convergence of the solution algorithms is important to ensure a physically correct wake solution that exhibits a grid-independent behavior with a desired order of accuracy.

Several examples of the application of free-vortex filament methods to helicopter rotor problems have been shown, including the wake structure and performance of single- and multirotor configurations, the flight in ground effect, the effects on the wake dynamics during maneuvering flight conditions, and the descending flight through the vortex ring state. Whereas free-vortex filament models used for helicopter rotor wake analyses have now reached a good level of maturity and predictive capability, further algorithmic improvements and better validation of the methods are still required. In particular, research is required to integrate more rigorously the blade wake and tip vortex rollup models and viscous effects (such as turbulent diffusion of vorticity) into vortex filament methods, while still retaining their relatively good computational efficiency.

References

[1]Leishman, J. G., *Principles of Helicopter Aerodynamics*, Cambridge Univ. Press, New York, 2000, Chap. 10.

[2]Shrinivasan, G. R., and Baeder, J. D., "TURNS: A Free-Wake Euler–Navier–Stokes Numerical Method for Helicopter Rotors," *AIAA Journal*, Vol. 31, No. 5, 1993, pp. 959–962.

[3]Landgrebe, A. J., "New Directions in Rotorcraft Computational Aerodynamics Research in the U.S.," CP-552, Aerodynamics and Acoustics of Rotorcraft, AGARD, 1994.

[4]McCroskey, W. J., "Vortex Wakes of Rotorcraft," AIAA Paper 95-0530, Jan. 1995.

[5]Tang, L., and Baeder, J. D., "Improved Euler Simulation of Hovering Rotor Tip Vortices with Validation," *Proceedings of the 55th Annual Forum of the American Helicopter Society International*, May 1999.

[6]Lewis, R. I., *Vortex Element Methods for Fluid Dynamic Analysis of Engineering Systems*, Cambridge Univ. Press, Cambridge, England, U.K., 1991.

[7]Cottet, G.-H., and Koumoutsakos, P. D., *Vortex Methods: Theory and Practice*, Cambridge Univ. Press, Cambridge, England, U.K., 2000.

[8]Crimi, P., "Theoretical Prediction of the Flow in the Wake of a Helicopter Rotor," Cornell Aeronautical Lab., Rept. BB-1994-5-1, Buffalo, NY, Sept. 1965.

[9]Landgrebe, A. J., "The Wake Geometry of a Hovering Rotor and its Influence on Rotor Performance," *Journal of the American Helicopter Society*, Vol. 17, No. 4, 1972, pp. 2–15.

[10]Kocurek, J. D., and Berkovitz, L. F., "Velocity Coupling: A New Concept for Hover and Axial Flow Wake Analysis and Design," CP-334, Prediction of Loads on Rotorcraft, AGARD, May 1982.

[11]Beddoes, T. S., "A Wake Model for High Resolution Airloads," *Proceedings of the 2nd International Conference on Basic Rotorcraft Research*, Univ. of Maryland, College Park, MD, Feb. 1985.

[12]Clark, D. R., and Leiper, A. C.,"The Free Wake Analysis—A Method for Prediction of Helicopter Rotor Hovering Performance," *Journal of the American Helicopter Society*, Vol. 15, No. 1, 1970, pp. 3–11.

[13]Scully, M. P., "A Method of Computing Helicopter Vortex Wake Distortion," Massachusetts Inst. of Technology, Rept. ASRL TR 138-1, Cambridge, MA, June 1967.

[14]Scully, M. P., "Computation of Helicopter Rotor Wake Geometry and Its Influence on Rotor Harmonic Airloads," Massachusetts Institute of Technology, Rept. ASRL TR 178-1, Cambridge, MA, March 1975.

[15]Sadler, S. G., "A Method for Predicting Helicopter Wake Geometry, Wake-Induced Inflow and Wake Effects on Blade Airloads," *Proceedings of the 27th Annual American Helicopter Society Forum*, May 1971.

[16]Miller, R. H., "A Simplified Approach to the Free Wake Analysis of a Hovering Rotor," *Vertica*, Vol. 6, 1982, pp. 89–95.

[17]Johnson, W., "A Comprehensive Analytical Model of Rotorcraft Aerodynamics and Dynamics, Part I: Analytical Development," NASA TM 81182, 1980.

[18]Lezius, D. K., "Analytical Solution for Inviscid Vortex Rollup from Elliptically Loaded Wings," *Journal of Aircraft*, Vol. 12, No. 11, 1975, pp. 911–914.

[19]Krasny, R., "Computation of Vortex Sheet Roll-Up in the Trefftz Plane," *Journal of Fluid Mechanics*, Vol. 184, 1987, pp. 123–155.

[20]Rule, J. A., and Bliss, D. B., "Prediction of Viscous Trailing Vortex Structure from Basic Loading Parameters," *AIAA Journal*, Vol. 36, No. 2, 1998, pp. 208–218.

[21]Bhagwat, M. J., and Leishman, J. G., "Correlation of Helicopter Tip Vortex Measurements," *AIAA Journal*, Vol. 38, No. 2, 2000, pp. 301–308.

[22]Ananthan, S., Leishman, J. G., and Ramaswamy, M., "The Role of Filament Stretching in the Free-Vortex Modeling of Rotor Wakes," *Proceedings of the American Helicopter Society 58th Annual National Forum*, June 2002.

[23]Crouse, G. L., Jr., and Leishman, J. G., "A New Method for Improved Rotor Free Wake Convergence," *31st AIAA Aerospace Sciences Meeting*, AIAA Paper 93-0872, Reno, NV, Jan. 1993.

[24]Bagai, A., and Leishman, J. G., "Rotor Free-Wake Modeling Using a Relaxation Technique—Including Comparisons with Experimental Data," *Journal of the American Helicopter Society*, Vol. 40, No. 3, 1995, pp. 29–41.

[25]Bhagwat, M., and Leishman, J. G., "Stability, Consistency and Convergence of Time Marching Free-Vortex Rotor Wake Algorithms," *Journal of the American Helicopter Society*, Vol. 46, No. 1, 2001, pp. 59–71.

[26]Lee, D. J., and Na, S. U., "Predictions of Airloads and Wake Geometry for Slowly Starting Rotor Blades in Hovering Flight by Using Time Marching Free Vortex Blob Method," *Proceedings of the 52nd Annual American Helicopter Society Forum*, May 1996.

[27]Bliss, D. B., and Miller, W. O., "Efficient Free Wake Calculations Using Analytical/Numerical Matching," *Journal of the American Helicopter Society*, Vol. 38, No. 2, 1993, pp. 53–60.

[28]Johnson, W., "A General Free Wake Geometry Calculation For Wings and Rotors," *Proceedings of the 51st Annual American Helicopter Society Forum*, May 1995.

[29]Bhagwat, M., and Leishman, J. G., "Accuracy of Straight-Line Segmentation Applied to Curvilinear Vortex Filaments," *Journal of the American Helicopter Society*, Vol. 46, No. 2, 2001, pp. 166–169.

[30]Bliss, D. B., Quackenbush, T. R., and Bilanin, A. J., "A New Methodology for Helicopter Free-Wake Analyses," *Proceedings of the 39th Annual Forum of the American Helicopter Society*, May 1983.

[31]Bliss, D. B., Dadone, L., and Wachspress, D. A., "Rotor Wake Modeling for High Speed Applications," *Proceedings of the 43th Annual American Helicopter Society Forum*, May 1987.

[32]Quackenbush, T. R., Wachspress, D. A., and Boschitsch, A. H., "Computation of Rotor Aerodynamic Loads with a Constant Vorticity Contour Free Wake Model," AIAA Paper 91-3229, Sept. 1991.

[33]Kaufmann, W., "Uber die Ausbreitung kreiszlindrischer Wirbel in zahen Flussigkeiten," *Ingenieur Archiv*, Vol. 31, No. 1, 1962, p. 1.

[34]Ogawa, A., *Vortex Flow*, CRC Series on Fine Particle Science and Technology, CRC Press, Boca Raton, FL, 1993.

[35]Miller, W. O., and Bliss, D. B., "Direct Periodic Solutions of Rotor Free Wake Calculations," *Journal of the American Helicopter Society*, Vol. 38, No. 2, 1993, pp. 53–60.

[36]Bagai, A., and Leishman, J. G., "Rotor Free-Wake Modeling Using a Psuedoimplicit Relaxation Algorithm," *Journal of Aircraft*, Vol. 32, No. 6, 1995, pp. 1276–1285.

[37]Bhagwat, M. J., and Leishman, J. G., "Stability Analysis of Rotor Wakes in Axial Flight," *Journal of the American Helicopter Society*, Vol. 45, No. 3, 2000, pp. 165–178.

[38]Leishman, J. G., and Bagai, A., "Challenges in Understanding the Vortex Dynamics of Helicopter Rotor Wakes," *AIAA Journal*, Vol. 36, No. 7, 1998, pp. 1130–1140.

[39]Quackenbush, T. R., Bliss, D. B., and Wachspress, D. A., "Computational Analysis of Hover Performance using a New Free Wake Method," *2nd International Conference on Rotorcraft Basis Research*, Univ. of Maryland, College Park, Feb. 1988.

[40]Miller, W. O., and Bliss, D. B., "Direct Periodic Solutions of Rotor Free Wake Calculations," *Proceedings of the 46th Annual American Helicopter Society Forum*, May 1990.

[41]Bagai, A., and Leishman, J. G., "Free-Wake Analysis of Tandem, Tilt-Rotor and Coaxial Rotor Configurations," *Journal of the American Helicopter Society*, Vol. 41, No. 3, 1996, pp. 196–207.

[42]Egolf, T. A., and Landgrebe, A. J., "Helicopter Rotor Wake Geometry and its Influence in Forward Flight, Vol. 1—Generalized Wake Geometry and Wake Effects in Rotor Airloads and Performance," NASA CR-3726, Oct. 1983.

[43]Jain, R., and Conlisk, A. T., "Interaction of Tip-Vortices in the Wake of a Two-Bladed Rotor in Axial Flight," *Journal of the American Helicopter Society*, Vol. 45, No. 3, 2000, pp. 157–164.

[44]Coyne, A. J., Bhagwat, M. J., and Leishman, J. G., "Investigation into the Rollup and Diffusion of Rotor Tip Vortices using Laser Doppler Velocimetry," *Proceedings of the 53rd Annual American Helicopter Society Forum*, May 1997.

[45]Vatistas, G. H., "New Model for Intense Self-Similar Vortices," *Journal of Propulsion and Power*, Vol. 14, No. 4, 1998, pp. 462–469.

[46]Vatistas, G. H., Kozel, V., and Mih, W. C., "A Simpler Model for Concentrated Vortices," *Experiments in Fluids*, Vol. 11, 1991, pp. 73–76.

[47]Bagai, A., and Leishman, J. G., "Flow Visualization of Compressible Vortex Structures Using Density Gradient Techniques," *Experiments in Fluids*, Vol. 15, 1993, pp. 431–442.

[48]Bhagwat, M. J., and Leishman, J. G., "On the Relationship between the Blade Lift and the Tip Vortex Characteristics," *Proceedings of the 54th Annual American Helicopter Society Forum*, May 1998.

[49]Squire, H. B., "The Growth of a Vortex In Turbulent Flow," *Aeronautical Quarterly*, Vol. 16, Aug. 1965, pp. 302–306.

[50]McAlister, K. W., Schuler, C. A., Branum, L., and Wu, J. C., "3-D Wake Measurements Near a Hovering Rotor for Determining Profile and Induced Drag," NASA TP-3577, 1995.

[51]Mahalingam, R., and Komerath, N. M., "Measurements of the Near Wake of a Rotor in Forward Flight," Paper AIAA 98-0692, 1998.

[52]Bhagwat, M. J., and Leishman, J. G., "Viscous Vortex Core Models for Free-Vortex Wake Calculations," *Proceedings of the 58th Annual Forum of the American Helicopter Society International*, June 2002.

[53]Wood, D. H., and Mayer, C., "Two New Methods for Calculating Velocities Induced by a Constant Diameter Far Wake," *Journal of Aircraft*, Vol. 28, No. 8, 1991, pp. 526–531.

[54]Radcliff, T. D., Burggraf, O. R., and Conlisk, A. T., "Axial Core Flow Effects on the Interaction of a Rotor-Tip Vortex with an Airframe," AIAA Paper 97-0658, Jan. 1997.

[55]Clark, D. R., and Leiper, A. C., "The Free Wake Analysis: A Method for the Prediction of Helicopter Hovering Peformance," *Proceedings of the American Helicopter Society 25th Annual National Forum*, May 1969.

[56]Egolf, T. A., "Rotor Wake Modeling for High Speed Applications," *Proceedings of the 44th Annual American Helicopter Society Forum*, May 1988.

[57]Brooks, T. F., Boyd, D. D., Burley, C. L., and Jolly, R. J., "Aeroacoustic Codes for Rotor Harmonic and BVI Noise-CAMRAD: Mod1/HIRES," AIAA Paper 96-1735, 1996.

[58]Bagai, A., and Leishman, J. G., "Adaptive Grid Sequencing and Interpolation Schemes for Rotor Free-Wake Analyses," *AIAA Journal*, Vol. 36, No. 9, 1998, pp. 1593–1602.

[59]Ghee, T. A., and Elliott, J. W., "The Wake of a Small-Scale Rotor Model in Forward Flight Using Flow Visualization," *Journal of the American Helicopter Society*, Vol. 40, No. 3, 1995, pp. 52–65.

[60]Dingeldein, R. C., "Wind Tunnel Studies of the Performance of a Multirotor Configurations," NACA TN 3236, 1954.

[61]Stepniewski, W. Z., "A Simplified Approach to the Aerodynamic Rotor Interference of Tandem Helicopter," *Proceedings of the American Helicopter Society West Coast Region Meeting*, Sept. 1955.

[62]Sweet, G. E., "Hovering Measurements for Twin-Rotor Configurations with and Without Overlap," NASA TN D-534, 1960.

[63]Stepniewski, W. Z., and Keys, C. N., *Rotary-Wing Aerodynamics*, Vol. 2, Dover, New York, 1984, Chap. 5.

[64]Bagai, A., and Leishman, J. G., "Free-Wake Analysis of Tandem, Tilt-Rotor and Coaxial Rotor Configurations," *Journal of the American Helicopter Society*, Vol. 40, No. 3, 1995, pp. 196–207.

[65]Griffiths, D. A., and Leishman, J. G., "A Study of Dual-Rotor Interference and Ground Effect Using a Free-Vortex Wake Model," *Proceedings of the 58th Annual Forum and Technology Display of the American Helicopter Society International*, June 2002.

[66]Saberi, H. A., and Maisel, M. D., "A Free-Wake Rotor Analysis Including Ground Effect," *Proceedings of the 43rd Annual American Helicopter Society Forum*, May 1987.

[67]Quackenbush, T. R., and Wachspress, D. A., "Enhancements to a New Free Wake Hover Analysis," NASA CR 177523, April 1989.

[68]Itoga, N., Nagashima, T., Iboshi, N., Kawakami, S., Prasad, J. V. R., and Peters, D. A., "Numerical Analysis of Ground Effect for a Lifting Rotor Hovering at Close Proximity to Inclined Flat Surface," *Proceedings of the American Helicopter Society Specialists' Meeting on Advanced Helicopter Technology and Disaster Relief*, April 1999.

[69]Sheridan, P. F., and Wiesner, W., "Aerodynamics of Helicopter Flight Near the Ground," *Proceedings of the 33rd Annual Forum of the American Helicopter Society*, May 1977.

[70]Rosen, A., and Isser, A., "A New Model for Rotor Dynamics During Pitch and Roll of a Hovering Helicopter," *Journal of the American Helicopter Society*, Vol. 40, No. 3, 1995, pp. 17–28.

[71]Keller, J. D., and Curtiss, H. C., "Modeling the Induced Velocity of a Maneuvering Helicopter," *Proceedings of the 52nd Annual American Helicopter Society Forum*, June 1996.

[72]Barocela, E., Peters, D. A., Kothapalli, K. R., and Prasad, J. V. R., "The Effect of Wake Distortion on Rotor Inflow Gradients and Off-Axis Coupling," AIAA Flight Mechanics Conf., AIAA Paper 97-3579, July 1997.

[73]Theodore, C., and Celi, R., "Flight Dynamic Simulation of Hingeless Rotor Helicopters Including a Maneuvering Free Wake Model," *Proceedings of the 54th Annual American Helicopter Society Forum*, May 1998.

[74]Bagai, A., Leishman, J. G., and Park, J., "Aerodynamic Analysis of a Helicopter in Steady Maneuvering Flight Using a Free-Vortex Rotor Wake Model," *Journal of the American Helicopter Society*, Vol. 44, No. 2, 1999, pp. 109–120.

[75]Drees, J. M., and Hendal, W. P., "The Field of Flow Through a Helicopter Rotor Obtained from Wind Tunnel Smoke Tests," *Journal of Aircraft Engineering*, Vol. 23, No. 266, 1951, pp. 107–111; also National Luchtvaart Laboratorium, Rept. A.1205, Feb. 1950.

[76]Castles, W., Jr., and Gray, R. B., "Empirical Relation Between Induced Velocity, Thrust, and Rate of Descent of a Helicopter Rotor as Determined by Wind-Tunnel Tests on Four Model Rotors," NASA TN-2474, Oct. 1951.

[77]Washizu, K., Azuma, A., Kōo, J., and Oka, T., "Experiments on a Model Helicopter Rotor Operating in the Vortex Ring State," *Journal of Aircraft*, Vol. 3, No. 3, 1966, pp. 225–230.

[78]Brinson, P., and Ellenrieder, T., "Experimental Investigation of Vortex Ring Condition," *Proceedings of the 24st Annual European Rotorcraft Forum*, Marseilles, France, Sept. 1998.

[79]Wolkovitch, J., "Analytical Prediction of Vortex-Ring Boundaries for Helicopters in Steep Descents," *Journal of the American Helicopter Society*, Vol. 17, No. 3, 1972, pp. 13–19.

[80]Heyson, H. H., "A Momentum Analysis of Helicopters and Autogyros in Inclined Descent, with Comments on Operational Restrictions," NASA TN D-7917, Oct. 1975.

[81]Leishman, J. G., Bhagwat, M. J., and Ananthan, S., "The Vortex Ring State as a Spatially and Temporally Developing Wake Instability," *Proceedings of the American Helicopter Society International Specialists Meeting on Aerodynamics, Acoustics and Test and Evaluation*, Jan. 2002.

[82]Leishman, J. G., Bhagwat, M. J., and Ananthan, S., "Free-Vortex Wake Predictions of the Vortex Ring State for Single-Rotor and Multi-Rotor Configurations," *Proceedings of the 58th Annual Forum and Technology Display of the American Helicopter Society International*, June 2002.